International Communications in Heat and Mass Transfer 177 (2026) 111532

Contents lists available at ScienceDirect

International Communications in Heat and Mass Transfer

journal homepage: www.elsevier.com/locate/ichmt

Analysis of the effects of perforated annular fins on thermal-hydraulic performance and vortex generation in a double-pipe heat exchanger

Zhihang Yan [a], Hiwa Najafi [a], Jong Boon Ooi [a,b], Boon Thong Tan [a], Foo Wah Low [c], James Ren [d], Cheen Sean Oon [a,*]

[a] Department of Mechanical Engineering, School of Engineering, Monash University Malaysia, Jalan Lagoon Selatan, Bandar Sunway 47500, Selangor, Malaysia
[b] Centre for Net-Zero Technology, Monash University Malaysia, Jalan Lagoon Selatan, Bandar Sunway 47500, Selangor, Malaysia
[c] Department of Electrical and Electronic Engineering, Lee Kong Chian Faculty of Engineering and Science, Universiti Tunku Abdul Rahman, 43000 Kajang, Selangor, Malaysia
[d] School of Engineering, Liverpool John Moores University, James Parsons Building, Byrom Street, L3 3AF Liverpool, UK

ARTICLE INFO

Keywords:
Heat transfer enhancement
Perforated annular fins
Longitudinal vortices
Transverse vortices
Thermal-hydraulic performance

ABSTRACT

Perforated structures are commonly incorporated into fins to enhance the thermal–hydraulic performance of heat exchangers. However, the influence of total porosity in perforated fins has often been overlooked in previous studies. Hence, this study conducts a systematic parametric analysis of the design of perforated annular fins, adopting a three-fold strategy: Design 1 varies the porosity by changing the hole number, Design 2 by changing the hole diameter, and Design 3 examines the combined influence of hole number and diameter while maintaining a fixed porosity. To obtain a high-fidelity numerical simulation of such complex turbulent flows, the SST k-ω turbulence model was adopted. Moreover, the numerical model is validated against empirical correlations and available experimental data. The results demonstrated that the introduction of perforations reduces the recirculation zone and transverse vortices behind the fins, while simultaneously disrupting the low velocity region upstream of the annular fins and generating additional local flow disturbances and longitudinal vortices. Both the average Nusselt number ($\overline{Nu}$) and pressure drop (Δp) decrease with the increase of porosity. However, when porosity is fixed, the increase in heat transfer enhancement and pressure drop caused by changes in the number and size of holes is limited, which means that porosity is the key factor dominating performance in this design. Furthermore, under the present fin geometry parameters, Reynolds number (Re) range, and thermal boundary conditions, a porosity of 0.2 provides the highest PEC value in this study, reaching 1.186 at $Re = 4540$.

1. Introduction

The growing global emphasis on energy efficiency and sustainable technologies has intensified the need for systems that are capable of efficient heat transfer. Since heat exchangers are central to most thermal processes, improving their performance is important for minimizing energy losses and enhancing the overall efficiency of the thermal system. Consequently, the growing need for energy-efficient systems has instigated comprehensive investigative endeavours to improve the performance of heat-transfer systems [1]. Double pipe heat exchangers (DPHEs) represent among the most widely used thermal devices in industry [2]. A DPHE consists of two concentric pipes that form separate flow passages, where heat is transferred across the inner wall through combined convection and conduction. Owing to their simple construction, ease of maintenance, mechanical robustness, and capability to operate under high-temperature and high-pressure conditions, DPHEs are widely applied in air-conditioning systems [3], power plants [4], and solar water-heating systems [5].

In contrast to active techniques that rely on external energy input to improve heat transfer, passive methods are extensively applied in DPHEs because of their simplicity, reliability, and energy-efficient operation [6]. Consequently, passive techniques have gained widespread research interest due to their effectiveness in enhancing heat transfer without additional energy input [7].

A range of passive enhancement techniques has been devised for the purpose of enhancing thermal performance, including surface or geometrical modifications [8,9], employing twisted tapes [10] or baffles [11], utilizing extended surfaces (fins) [12], and using nanofluids [13,14]. Perforated louvered strip inserts have also been employed by

* Corresponding author.
E-mail address: oon.cheensean@monash.edu (C.S. Oon).

https://doi.org/10.1016/j.icheatmasstransfer.2026.111532

Available online 16 May 2026

Nomenclature

A_{fin}	Projected area of a non-perforated fin (m^2)
C_p	Specific heat capacity (J/(kg·K))
D_f	Diameter of the hole (mm)
D_h	Hydraulic diameter of annular channel (mm)
D_ω	Cross-diffusion term (kg/(m^3·s))
F	Safety factor
f	Friction factor
GCI	Grid convergence index
$\widetilde{P_k}$	Production of turbulent kinetic energy (kg/(m·s^3))
g	Gravity (m/s^2)
K	Thermal conductivity (W/(m·K))
k	Turbulent kinetic energy (m^2/s^2)
N	Number of perforation holes
Nu	Local Nusselt number
$\overline{Nu}$	Average Nusselt number
PEC	Performance evaluation criterion
p	Pressure (Pa)
Pr	Prandtl number (Laminar)
Pr_t	Prandtl number (Turbulent)
q''	Heat flux density (W/m^2)
Re	Reynolds number
T	Temperature (K)
T_b	Bulk fluid temperature (K)
T_w	Surface temperature (K)
u_i	Velocity (m/s)

Greek symbols

ε	Relative error (grid convergence)
μ	Molecular dynamic viscosity (Pa·s)
μ_t	Turbulent dynamic viscosity (Pa·s)
σ_k	Turbulent Prandtl number of k
σ_ω	Turbulent Prandtl number ofω
φ	Porosity (fin open-area ratio)
Φ	Variable value calculated (grid convergence)
ω	Specific turbulent dissipation rate (1/s)

Subscripts

0	Smooth pipe (no-fins baseline)
i	Inner
o	Outer
in	Inlet
out	Outlet
w	Wall

Nakhchi et al. [15] to enhance thermal-hydraulic performance. Their study revealed that the main reason for the average Nusselt number ($\overline{Nu}$) enhancement was the additional vortex flow generated near the perforations. In another investigation, Wang et al. [16] reported that employing sinusoidal vortex generators in an annular heat exchanger resulted in a 20.4% increase in the $\overline{Nu}$ compared with a smooth pipe. Moreover, Dhavale and Lele [17] analysed the impact of high-porosity metallic foams in a DPHE and concluded that the best performance was achieved using 30 pores-per-inch (PPI) aluminum foam. In a separate study, Said et al. [18] proposed a double-helical pipe heat exchanger combined with nanofluids and perforated curved turbulators. The results showed that the configuration without turbulators achieved a higher thermal performance factor than the other cases, owing to the significant pressure drop (Δp) that was observed in cases employing turbulators. Therefore, optimizing the DPHE configuration to achieve higher heat transfer with lower Δp remains a critical challenge.

Building upon these enhancement strategies, the use of fins has also been extensively explored to improve the thermal performance of DPHEs. Among different fin geometries, longitudinal [19], radial [20], and helical configurations [21] of the fins are the most widely used. Beyond enlarging the effective heat transfer area, fins can enhance flow disturbance and enhance local convection by reducing the boundary layer thickness. Certain fin geometries can even induce secondary or swirling flows, further improving overall heat transfer performance [22]. However, the incorporation of fins unavoidably increases flow resistance, leading to higher Δp and greater pumping power requirements. As a result, recent research has focused on innovative fin geometries and hybrid designs that maximize heat transfer efficiency while minimizing hydraulic losses.

Researchers have proposed various geometric optimization strategies for fin design, including perforation [23], interruption [19], corrugation [24], and twisting [25]. Among these, perforation has received considerable research attention because it can alleviate flow resistance while maintaining or even slightly improving heat transfer performance [26]. Shaeri and Jen [27] investigated the influence of perforation size and number on thermal-hydraulic performance of perforated fin arrays at a fixed porosity of 0.44. Their analysis showed that fins with fewer but larger perforations exhibited greater performance in enhancing the heat transfer rate than those with a higher number of smaller perforations. Sheikholeslami and Ganji [28] also examined the influence of the number of perforations in a DPHE equipped with perforated turbulators. The results showed that the highest thermal performance was provided for the turbulator design containing eight holes with an open-area ratio of 0.07. Although the diameter of individual holes was fixed in their study to eliminate their influence, the identified optimum, which consists of eight holes and an open-area ratio of 0.07, corresponds to the upper limit of the parameter range investigated. Consequently, it remains uncertain whether higher thermal performance could be achieved beyond the range studied by further increasing the total open area or the number of perforations. Wang et al. [29] investigated the thermal-hydraulic characteristics of an annular channel equipped with annular fins containing different numbers of perforations (ranging from 0 to 16) and found that the configuration with eight perforations provided the highest performance evaluation criterion value. However, in their study, variations in hole geometry and diameter accompanied the change in hole number, which also influenced the overall thermal-hydraulic performance. Since these factors were not isolated in their analysis, it is difficult to determine whether the observed enhancement was truly attributable to the variation in hole number alone. Recently, Song et al. [30] proposed a DPHE equipped with a perforated helical fin on the annulus side and numerically investigated the influence of perforation diameter (0–12 mm) on flow behaviour and thermal efficiency under turbulent conditions. Their results show that the perforation diameter significantly affects the overall thermal performance.

In previous studies on perforated fins, most researchers focused on the influence of either the number or the size of perforations. Individual investigations often examined only a single variable while keeping others constant [23]. Furthermore, many previous studies regarded porosity, also referred to as the total open-area ratio, as a dependent result of varying hole number or diameter, and its independent influence was not explicitly analysed. Consequently, systematic investigations that concurrently evaluate the roles of porosity, hole number, and hole diameter in determining the thermal-hydraulic performance of perforated fin configurations remain limited.

The present study numerically investigates a DPHE equipped with perforated annular fins. The effects of porosity (0.1–0.5), hole number

(3–18), and hole diameter (0.904–2.215 mm) on flow behaviour and heat transfer performance are systematically evaluated to provide a comprehensive understanding of the newly developed DPHE. Three design strategies are adopted to examine the effect of porosity on the thermal-hydraulic behaviour of the perforated fins, forming a three-fold approach: Design 1 varies the porosity by changing the hole number, Design 2 varies the porosity by changing the hole diameter, and Design 3 examines the combined influence of hole number and diameter while maintaining a fixed porosity. In Design 3, the parametric study is carried out at the optimal porosity identified from the first two designs. The findings of this study highlight the critical role of porosity in governing the thermal-hydraulic performance of perforated annular fins. Under the present geometric configuration and boundary conditions, an optimal porosity is identified within the investigated range. However, when the porosity is fixed, varying the hole number and hole diameter leads to only a minor influence on the heat transfer enhancement and flow characteristics. These results suggest that an optimal porosity should be identified before further geometric optimization of perforated fins. This study provides useful guidance for the design and optimization of perforated annular fins.

2. Problem definition

2.1. Geometric configuration

This study focuses on the numerical analysis of a DPHE equipped with perforated annular fins to evaluate its thermal-hydraulic performance under turbulent flow conditions. Fig. 1 illustrates the geometric configuration of the DPHE model and the computational domain employed in this study. As can be seen in Fig. 1(a), the overall schematic illustrates the DPHE, where the red and blue regions represent the hot fluid flowing through the inner pipe and the cold fluid in the outer annulus, respectively. The rectangular outline indicates the computational domain extracted for simulation.

Under practical operating conditions, a double pipe heat exchanger (DPHE) comprises two solid components, namely the inner and outer pipes, together with two fluid domains: a hot fluid flowing inside the inner tube and a cold fluid occupying the annular region. As the present study focuses on the influence of perforated annular fins on the heat transfer and flow behaviour of the cold-side fluid, the hot fluid is replaced by a uniform heat flux imposed on the inner surface of the inner pipe. The outer pipe is modelled as an adiabatic wall to prevent heat loss. These simplification strategies for the outer and the inner pipe have been adopted in similar studies [19,30].

In numerical studies, simplifying the outer pipe as an adiabatic surface exhibits consistency with actual experimental operations. In experimental studies, insulation materials are usually wrapped around the outer pipe to minimize heat exchange between the test section and the external environment [31]. However, in practical engineering applications, a temperature difference between the outer pipe wall and the ambient environment usually persists. Consequently, minor heat exchange between the outer wall and the environment is unavoidable. This heat transfer primarily occurs through natural convection and thermal radiation.

Using a uniform heat flux instead of the heat flow ignores the thermal interaction between the cold and hot fluids and the redistribution effect of the wall heat flux along the axial direction. Therefore, the local wall temperature distribution may differ from the actual operation of DPHE, which is one of the limitations of this study. Currently, the dominant mechanism of heat transfer enhancement mainly stems from the flow reconstruction induced by the geometric structure of perforated fins, the formation of vortex structures, and the disturbance of the near-wall

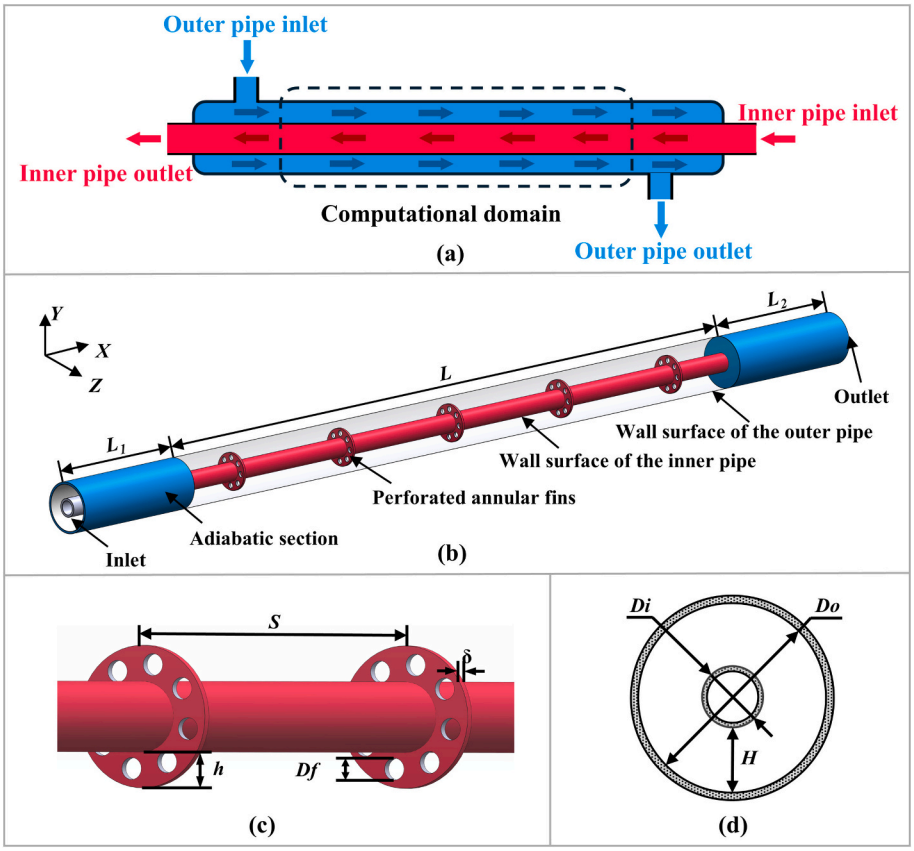

Fig. 1. (a) Schematic of the concentric DPHE and the selected computational domain. (b) Detailed view of the computational domain. (c) Enlarged view of the perforated annular fin. (d) Cross-sectional view of the double pipe.

boundary layer. The coupling between heat transfer enhancement and the redistribution of axial heat flux on the hot side is relatively limited. Under the same thermal boundary conditions, the application of uniform thermal flux boundary conditions usually does not significantly alter the relative thermal-hydraulic performance trends among different configurations [32,33]. Therefore, the conclusions of this study should be understood as relative design guidance under the current thermal boundary conditions, rather than absolute performance predictions for specific actual operating conditions of the DPHE.

Fig. 1(b) depicts the computational domain used for numerical simulation. The total length of the model is 1400 mm, while the length of the testing section (L) is 1000 mm. Two adiabatic sections (L_1 and L_2), each 200 mm long, are positioned at the inlet and outlet to eliminate the effects of flow development at the entrance and exit regions. Five perforated annular fins are mounted on the outer surface of the inner pipe within the testing section. The first fin is located 300 mm downstream of the inlet, and the spacing (S) between consecutive fins is 200 mm. Fig. 1(c) presents an enlarged view of the finned region, and Fig. 1 (d) shows the cross-section of the DPHE. The geometric parameters of the configuration are summarized in Table 1.

2.2. Boundary conditions and material properties

For the annular channel, the inlet flow rate ranges from 8 to 20 L/min, corresponding to Reynolds numbers (Re) between 4540.33 and 11,350.76. The inlet temperature of the cold fluid is fixed at 303.15 K. To define the flow condition, a velocity inlet boundary condition was applied at the entrance, while a pressure outlet with zero-gauge pressure was imposed at the exit. A uniform heat flux of 16,323.58 W/m^2, equivalent to a total input power of 500 W, is applied to the inner surface of the inner pipe, whereas the outer pipe wall is assumed to be adiabatic. All solid-fluid interfaces were treated as coupled walls to ensure continuity of temperature and heat flux between the solid and fluid domains.

In the present study, the temperature range of the working fluid is relatively small. Therefore, the variations in thermophysical properties caused by temperature changes are considered negligible, and the thermal-physical properties of both the fluid and solid are assumed to be constant. The working fluid used in the simulation is distilled water [34], while the solid regions, including the inner pipe and fins, are made of steel. The thermophysical properties of the materials are summarized in Table 2. It should be noted that when the temperature variation of the fluid is large, the viscosity of the fluid will change significantly. This variation may affect the velocity gradients near the fluid-solid interface and influence the development of the thermal boundary layer. In addition, viscosity variations will also influence the pressure drop characteristics of the flow. Under such conditions, the assumption of constant thermal-physical properties may no longer be reasonable.

Table 1
Summary of the geometrical details.

Geometrical parameter	Value
Testing region length, L (mm)	1000
Entrance/Exit extension length, L_1, L_2 (mm)	200
Total pipe length, $L_1 + L + L_2$ (mm)	1400
Inner pipe outer diameter, D_i (mm)	12.75
Outer pipe inner diameter, D_o (mm)	32.15
Annular channel height, H (mm)	9.7
Fin spacing, S (mm)	200
Fin thickness, δ (mm)	1.5
Fin height, h (mm)	2.425
Hole number, N	3–18
Hole diameter, D_f (mm)	0.904–2.215
Porosity,φ	0.1–0.5

Table 2
The relevant physical parameters of the working fluid and solid material.

Property	Distilled water	Steel
Density, ρ (kg/m^3)	995.5	8030
Viscosity, μ (Pa·s)	0.000829	–
Thermal conductivity, K (W/(m·K))	0.611	16.27
Specific heat capacity, C_p (J/(kg·K))	4142	502.48
Prandtl number, Pr	5.62	–

3. Numerical model

3.1. Governing equations

The present study considered a three-dimensional, steady-state fluid flow and heat transfer process within the computational domain. The working fluid was assumed to be incompressible and Newtonian. Under these conditions, the governing equations for the conservation of mass, momentum, and energy can be expressed in tensor form in the Cartesian coordinate system as follows [35,36]:

Continuity equation:

$$\frac{\partial(\rho u_i)}{\partial x_i} = 0 \tag{1}$$

Momentum equation:

$$\frac{\partial(\rho u_i u_j)}{\partial x_j} = -\frac{\partial p}{\partial x_i} + \frac{\partial}{\partial x_j}\left[(\mu+\mu_t)\left(\frac{\partial u_i}{\partial x_j}+\frac{\partial u_j}{\partial x_i}\right)\right] - \frac{\partial}{\partial x_i}\left(\frac{2}{3}\rho k\right) + \rho g_i \tag{2}$$

Energy equation:

$$\frac{\partial(\rho C_p u_i T)}{\partial x_i} = \frac{\partial}{\partial x_j}\left[\left(\frac{\mu C_p}{Pr}+\frac{\mu_t C_p}{Pr_t}\right)\frac{\partial T}{\partial x_j}\right] \tag{3}$$

This energy equation describes the heat transfer process in the fluid domain. Since heat transfer occurs across the fluid-solid interface, conjugate heat transfer is considered in the numerical model. The temperature field in the solid domain is governed by the steady-state heat conduction equation.

$$\frac{\partial}{\partial x_i}\left(k_s\frac{\partial T}{\partial x_i}\right) = 0 \tag{4}$$

At the interface between the fluid and solid domains, the continuity of temperature and heat flux is imposed to ensure thermal coupling between the two regions.

$$T_f = T_s \tag{5}$$

$$k_f\frac{\partial T_f}{\partial n} = k_s\frac{\partial T_s}{\partial n} \tag{6}$$

where ρ is the fluid density, u_i represents the velocity component in the i-direction, p denotes pressure, T is temperature, and C_p is the specific heat capacity of the fluid. The parameters μ and μ_t represent the molecular and turbulent dynamic viscosities, respectively. Pr and Pr_t denote the laminar and turbulent Prandtl numbers.

In the present simulations, the turbulent Prandtl number Pr_t is assumed to be constant and set to 0.85, which is a commonly adopted value for turbulent heat transfer in internal flows. This assumption has been widely used in numerical studies of turbulent forced convection and has been shown to provide reasonable agreement with experimental observations [37,38].

3.2. Turbulence model

To close the system of Reynolds-Averaged Navier-Stokes (RANS) equations presented in the previous section, a turbulence model is required to determine the turbulent viscosity (μ_t). In this study, the Shear Stress Transport (SST) k-ω model was employed. This model is

well known for its accuracy and robustness in predicting flows with adverse pressure gradients and flow separation conditions relevant to the complex wake and vortex structures generated by the perforated fins. The SST k-ω model combines the robustness of the standard k-ω formulation in the near-wall region with the free-stream independence of the k-ε model, thereby providing reliable results for flows involving separation and strong shear layers. Moreover, this model has been recommended in the literature for similar applications involving complex fin geometries and perforated surfaces, confirming its suitability for the present simulation [30]. The transport equations for the turbulent kinetic energy (k) and the specific dissipation rate (ω) are given as [39]:

$$\frac{\partial}{\partial x_i}(\rho k u_i) = \frac{\partial}{\partial x_i}\left[\left(\mu + \frac{\mu_t}{\sigma_k}\right)\frac{\partial k}{\partial x_i}\right] + \widetilde{P_k} - \rho\beta^* k\omega \tag{7}$$

$$\frac{\partial}{\partial x_i}(\rho \omega u_i) = \frac{\partial}{\partial x_i}\left[\left(\mu + \frac{\mu_t}{\sigma_\omega}\right)\frac{\partial \omega}{\partial x_i}\right] + \frac{\alpha}{v_t}\widetilde{P_k} - \rho\beta\omega^2 + D_\omega \tag{8}$$

where P_k denotes the production term of turbulent kinetic energy, and D_ω is the cross-diffusion term defined as:

$$\mu_t = \frac{\rho k}{\omega}\frac{1}{max\left[\frac{1}{\alpha^*}, \frac{SF_2}{a_1\omega}\right]} \tag{9}$$

$$\widetilde{P_k} = min(P_k, 10\rho\beta^* k\omega) \tag{10}$$

$$P_k = -\rho\overline{u_i' u_j'}\frac{\partial u_j}{\partial x_i} \tag{11}$$

$$D_\omega = 2(1-F_1)\rho\frac{1}{\omega\sigma_{\omega,2}}\frac{\partial k}{\partial x_j}\frac{\partial \omega}{\partial x_j} \tag{12}$$

Further details regarding the above equations can be found in Ref. [40].

4. Numerical method

4.1. Performance parameters

To evaluate the overall thermal-hydraulic performance, the following dimensionless parameters and performance criteria were used. In the numerical post-processing, the flow domain was discretized into a series of cross-sectional planes along the axial direction. The local thermal-hydraulic quantities were evaluated at each cross-section to obtain the local and averaged performance parameters for each operating condition.

The local heat transfer coefficient was calculated by Eq. (13):

$$h(x_i) = \frac{q''(x_i)}{T_w(x_i) - T_b(x_i)} \tag{13}$$

where $q''(x_i)$ is the local wall heat flux on the heat transfer surface at the axial location x_i, $T_w(x_i)$ is the wall temperature of the heat transfer surface, and $T_b(x_i)$ is the bulk fluid temperature at the axial location x_i, obtained from the mass-weighted average fluid temperature over the corresponding cross-section, which can be determined by Eq. (14).

$$T_b(x_i) = \frac{\int_A \rho u T\, dA}{\int_A \rho u\, dA} \tag{14}$$

where ρ is the fluid density, u is the local axial velocity of the fluid, T is the local fluid temperature, and A is the cross-sectional area of the flow domain.

The average heat transfer coefficient was obtained by axial integration of the local heat transfer coefficient along the test section:

$$\overline{h} = \frac{1}{L}\int_0^L h(x)dx \tag{15}$$

Moreover, the local Nusselt number (Nu) and the average Nusselt number ($\overline{Nu}$) were calculated by Eqs. (16) and (17).

$$Nu(x_i) = \frac{h(x_i)D_h}{K} \tag{16}$$

$$\overline{Nu} = \frac{1}{L}\int_0^L Nu(x)dx \tag{17}$$

$$D_h = \frac{4A}{P} \tag{18}$$

where K is the thermal conductivity of the fluid, D_h is the hydraulic diameter, A is the cross-sectional area of the fluid, and P is the wetted perimeter. For a smooth concentric annular flow channel, substituting the corresponding expressions for the cross-sectional area and wetted perimeter yields Eq. (19).

$$D_h = D_o - D_i \tag{19}$$

where D_o is the inner diameter of outer pipe, D_i is the outer diameter of inner pipe. In the present study, although the incorporation of perforated fins alter the actual flow area and the wetted perimeter, to ensure consistent comparison between different configurations, the hydraulic diameter derived from the annular gap is adopted as the characteristic scale under all operating conditions. This simplification approach has also been widely adopted in similar studies [41,42], and it does not change the relative performance trends between configurations.

The Reynolds number, pressure drop, and friction factor, which characterize the flow regime and hydraulic performance of the DPHE, were determined using Eqs. (20)–(22), respectively.

$$Re = \frac{\rho U D_h}{\mu} \tag{20}$$

$$\Delta p = p_{in} - p_{out} \tag{21}$$

$$f = \frac{\Delta P D_h}{2\rho u^2 L} \tag{22}$$

where p_{in} and p_{out} denote the pressures measured at the inlet and outlet of the test section, respectively, rather than the overall Δp across the entire flow domain.

The overall thermal-hydraulic performance of the enhanced surface was evaluated using the performance evaluation criterion (PEC) [43], originally proposed by Webb and Kim [44], as defined in Eq. (23). Although the PEC formulation was originally derived based on the assumptions of equal pumping power and fully developed flow, it has been widely adopted in heat transfer enhancement studies as a relative performance indicator [21,45]. It can evaluate the overall thermal-hydraulic performance of enhanced heat transfer systems by considering both heat transfer enhancement and the pressure drop penalty. In the present study, the PEC is employed as a relative performance indicator to compare different perforated annular fin configurations under consistent operating conditions, rather than as an absolute measure of the thermal-hydraulic performance of a practical heat exchanger.

$$PEC = \frac{(\overline{Nu}/\overline{Nu_0})}{(f/f_0)^{1/3}} \tag{23}$$

where $\overline{Nu}$ and f are the average Nusselt number and friction factor for the pipe with fins, while $\overline{Nu_0}$ and f_0 corresponds to those of the pipe without fins under the same Re. A PEC greater than 1 indicates an overall improvement in thermal-hydraulic performance. It has been demonstrated that the enhancement of heat transfer is greater than the rise in flow resistance. A PEC less than 1 means that the Δp penalty is dominant, leading to poorer thermal-hydraulic performance.

4.2. Numerical settings and convergence

The numerical simulations were carried out using ANSYS Fluent 2022 R1, which employs the finite volume method to discretize and solve the governing equations. The pressure-velocity coupling was handled using the SIMPLEC algorithm to enhance the convergence rate. The pressure term was discretized using a second-order scheme, while the momentum, energy, turbulent kinetic energy, and specific dissipation rate equations were solved using the second-order upwind scheme. The gradients were computed using the least-squares cell-based method, and the Rhie-Chow momentum interpolation was applied to prevent pressure-velocity decoupling. For convergence control, the scaled residuals of all governing equations were monitored, with the convergence criteria set to 10^{-10} for the energy equation and 10^{-6} for all other equations.

4.3. Mesh generation and grid independence test

A hybrid poly-hexcore mesh was employed in the computational domain, consisting of both polyhedral and hexahedral cells. Polyhedral cells were generated near the fin and tube walls to accurately capture the boundary layer and complex perforated geometry, while hexahedral core cells were used in the bulk flow region to reduce the total element count and improve computational efficiency. As shown in Fig. 2, a smooth transition between the near-wall polyhedral region and the hexahedral core region can be clearly observed. In this study, the mesh generation strategy distinguishes between the core flow region and the near-wall region. In the grid-independence study, the global mesh size governed the element scale in the core flow domain and was systematically refined, which primarily determined the total number of mesh elements. Inflation layers were applied to resolve the steep velocity and temperature gradients near the wall surface. The first-layer thickness was set to 0.03 mm on the pipe surface and 0.01 mm on the fin surface. The inflation layers were generated with a growth rate of 1.2 and a total of 12 layers, ensuring that the dimensionless wall distance (y^+) remained below 1 throughout the domain. The inflation-layer parameters were kept constant for all grid levels and were not included in the global mesh refinement.

The mesh was refined at four levels to assess grid independence. The minimum global element sizes for the coarse, intermediate, fine, and very fine meshes were 0.4 mm, 0.2 mm, 0.1 mm, and 0.05 mm, respectively. The $\overline{Nu}$ and Δp were chosen as evaluation parameters. The grid convergence index (*GCI*) method was used to quantify the discretization error and verify that the solutions fell within the asymptotic convergence range [46]. The *GCI*, relative error (ε), and order of convergence (P) were computed as:

$$GCI = \frac{|F|\varepsilon}{r^p - 1} \tag{24}$$

$$\varepsilon = \frac{\phi_2 - \phi_1}{\phi_1} \tag{25}$$

$$P = \frac{ln\left(\frac{\phi_3 - \phi_2}{\phi_2 - \phi_1}\right)}{ln(r)} \tag{26}$$

where F, ε, Φ, P, and r denote the safety factor, relative error, selected variable, order of convergence, and grid refinement ratio, respectively. The safety factor F was set to 1.25 for all refinements, and the grid refinement ratio was set to 2.

The grid independence test was performed under the representative condition of 18 perforations, 0.2 porosity, and a flow rate of 20 L/min (Re = 11,350). The results are summarized in Table 3, and the corresponding trends of the $\overline{Nu}$ and Δp with mesh refinement are illustrated in Fig. 3. As shown in this figure, both the $\overline{Nu}$ and the Δp increases with mesh refinement. Although the variation in $\overline{Nu}$ becomes negligible beyond the intermediate mesh, the Δp still shows a slight increase as the mesh becomes finer due to improved wall-resolution accuracy. When the total number of elements exceeded approximately 1.2×10^7, the variations in $\overline{Nu}$ and Δp became insignificant. The corresponding *GCI* values between fine and very fine meshes are $GCI_{\overline{Nu}} = 0.075\%$ and $GCI_{\Delta p} = 0.520\%$, confirming that the solution lies within the range of convergence. Therefore, the fine mesh was chosen for all subsequent simulations, which can ensure a good balance between accuracy and computational efficiency.

4.4. Validation of numerical model

To validate the accuracy of the numerical model, the calculated results of the $\overline{Nu}$ and f for the smooth double pipe configuration are compared with both classical empirical correlations and available experimental data. For the correlation-based comparison, the $\overline{Nu}$ and f are evaluated using widely accepted correlations for turbulent flow and heat transfer, developed by Gnielinski [47] and Petukhov [48]. Relative

Table 3
Mesh refinement levels and corresponding *GCI* results for the grid independence test.

Mesh refinement	Number of elements	Min. global element size (mm)	Average Nusselt number	Pressure drop (Pa)
Coarse	2,391,122	0.4	116.733	312.753
Intermediate	6,156,392	0.2	120.203	316.487
Fine	12,291,271	0.1	120.952	318.772
Very fine	19,598,774	0.05	121.214	319.616
Extrapolated values			121.286	320.946

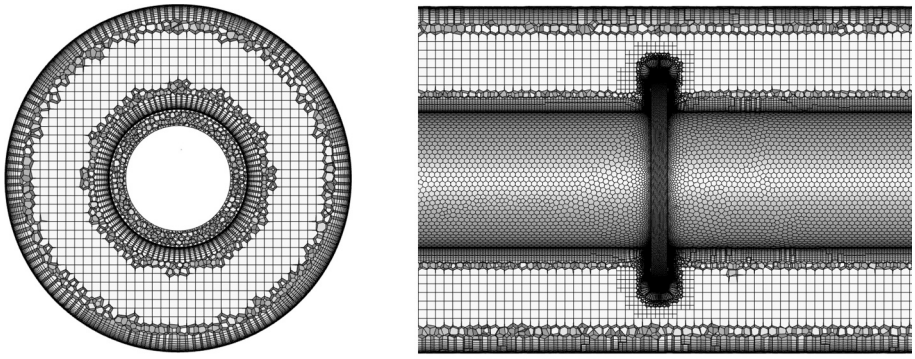

(a) **(b)**

Fig. 2. Grid schematic diagram; (a) cross-sectional view of the computational domain and (b) detailed mesh structure around the perforated fin.

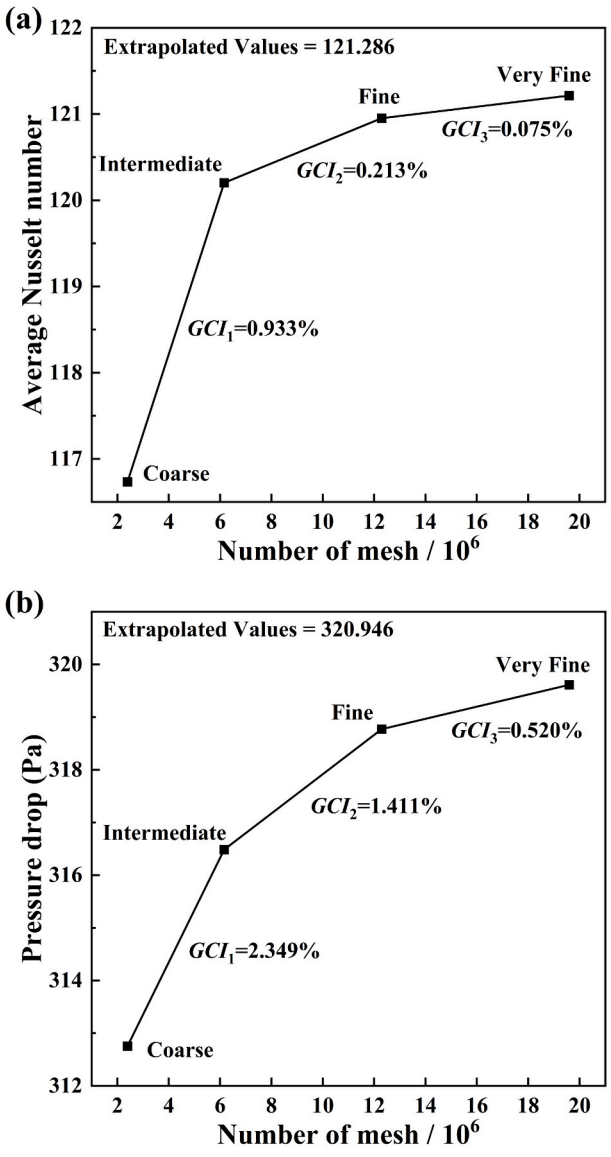

Fig. 3. Variation of (a) $\overline{Nu}$ and (b) Δp with mesh refinement at Re = 11,350.

equations are defined in Eqs. (27)–(34)

$$Nu_{Pe} = \frac{\left(\frac{f_{ann}}{8}\right) Re^{*} Pr}{k_1 + 1.27 + (f_{ann}/8)^{\frac{1}{2}} \left(Pr^{\frac{2}{3}} - 1\right)} \left(1 + \left(\frac{D_h}{L}\right)^{\frac{2}{3}}\right) F_{ann}\, K^{*} \tag{27}$$

where f_{ann} is the friction factor for annular flow, calculated by Eq. (24):

$$f_{ann} = \left(1.8 log_{10} Re^{*} - 1.5\right)^{-2} \tag{28}$$

The modified Reynolds number Re^{*} is defined by Eq. (25):

$$Re^{*} = Re \frac{(1+a^2) ln(a) + (1-a^2)}{ln(a) + (1-a^2)} \tag{29}$$

$$a = \frac{D_i}{D_o} \tag{30}$$

The empirical coefficients k_1, F_{ann}, and K^{*} are calculated by Eqs. (27), (28), and (29):

$$k_1 = 1.07 + \frac{900}{Re} - \frac{0.63}{1 + 10Pr} \tag{31}$$

$$F_{ann} = 0.9 - 0.15 a^{0.6} \tag{32}$$

$$K^{*} = \left(\frac{Pr_b}{Pr_{wall}}\right)^{0.11} \tag{33}$$

where Pr_b and Pr_{wall} are the Prandtl numbers evaluated at the bulk and wall temperatures.

$$f_{Pe} = (0.79 ln Re - 1.64)^{-2} \tag{34}$$

Further validation is also performed using the physical experimental data from Hosseini et al. [49]. In their study, distilled water was used as the working fluid, with thermophysical properties identical to those in the present work. The inner and outer pipe diameters were 15 mm and 25.7 mm, respectively, and the total length was 900 mm, including a 600 mm heated test section. A constant heat input of 900 W was supplied to the inner tube through an electric heater, while the cold fluid entered the annulus at 303.15 K. The Re ranged from 3065 to 7954.

Fig. 4 presents the validation results: subplot (a) compares the numerical results with the empirical correlations, while subplot (b) shows the comparison with available experimental data. As shown in Fig. 4(a), the calculated $\overline{Nu}$ and f follow closely the trends of the correlations. For

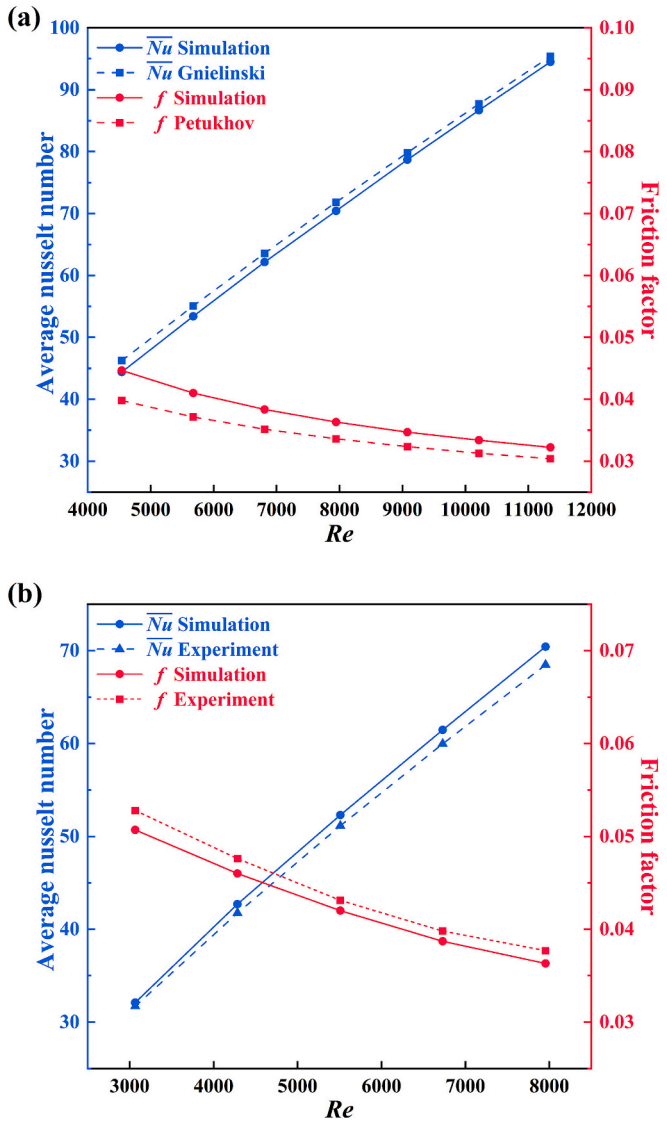

Fig. 4. Comparison of simulated results with (a) empirical correlations and (b) experimental data [49].

instance, the simulation results of the $\overline{Nu}$ align closely with Gnielinski's correlation, showing a maximum deviation of 3.95%. Regarding the f comparison, the simulation results are slightly higher than the empirical correlation at lower Re. However, at higher Re, the results show much better agreement, and overall, the validation indicates that the simulation is accurate and reliable. In addition, Fig. 4(b) demonstrates good agreement between the numerical results and the experimental measurements, with maximum deviations of the $\overline{Nu}$ and f between the current simulation and the experimental data of approximately 2.85% and 4.12%, respectively. These results confirm that the present model accurately captures the heat transfer and flow characteristics of the DPHE.

4.5. Verification of fully developed inlet flow

In a real flow field within a pipe, the velocity of the core flow is higher, while the velocity near the wall gradually decreases to zero due to the no-slip condition [50]. However, in the numerical model, a uniform velocity profile normal to the inlet surface is typically applied at the inlet boundary to simplify the boundary condition. As a result, the flow near the inlet is not immediately fully developed, and a certain adiabatic entrance section is required so that the boundary layer can grow and the velocity profile can evolve into the correct parabolic or turbulent distribution before entering the test section [51]. To obtain a hydrodynamically fully developed inflow, an adiabatic entrance section with a length of 200 mm is provided upstream of the heated test section. Velocity profiles are sampled at several axial positions along this entrance region for investigation.

Fig. 5 shows the axial evolution of velocity profiles at several positions along the entrance and at a location within the test section for the smooth pipe case under a flow rate of 20 L/min (Re = 11,350). As shown in this figure, the velocity distributions gradually converge and eventually collapse onto a single profile, demonstrating that hydrodynamic development is achieved within the entrance section. Therefore, the reserved adiabatic section length of 200 mm is sufficient to provide a fully developed inflow.

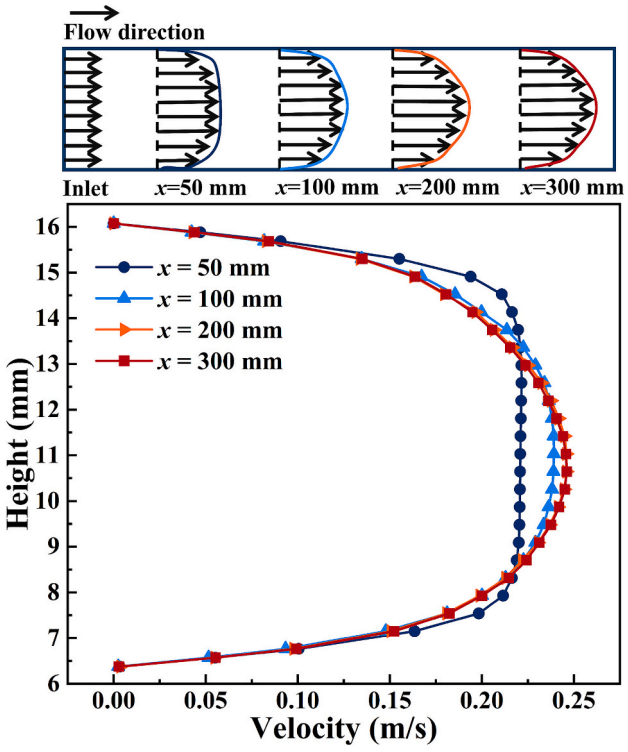

Fig. 5. Axial evolution of velocity profiles for verification of fully developed inlet flow at Re = 11,350.

5. Results and discussions

5.1. Design of fins

The fins used in this study are circular annular fins attached to the outer surface of the inner pipe. Each fin contains uniformly distributed circular perforations to generate a range of porosities. The porosity (φ) is defined as the ratio of the total open-hole area to the total projected area of a single fin, expressed as:

$$\varphi = \frac{N\pi\left(D_f/2\right)^2}{A_{\text{fin}}} \tag{35}$$

where N is the number of holes, D_f is the hole diameter, and A_{fin} represents the projected area of a non-perforated fin in the flow direction. In this expression, the hole number (N) and the hole diameter (D_f) are independent geometric variables. A change in either of these variables will alter the porosity (φ).

To systematically examine the effect of porosity on the overall thermal-hydraulic performance, three different fin design strategies are proposed, adopting a three-fold approach: Design 1 varies the porosity by changing the hole number, Design 2 varies the porosity by changing the hole diameter, and Design 3 examines the combined influence of hole number and diameter while maintaining a fixed porosity.

5.1.1. Design 1

In Design 1, the hole diameter is fixed at 2.215 mm, and the number of holes is varied through the values 3, 6, 9, 12, and 15 to achieve corresponding porosities of 0.1, 0.2, 0.3, 0.4, and 0.5. A relatively large hole diameter is selected to minimize the influence of the hole size itself, so that the variation in flow and heat transfer can be attributed mainly to the change in the number of perforations. The fin geometries corresponding to these configurations are illustrated in Fig. 6(a).

5.1.2. Design 2

In Design 2, the hole number is held constant at 18, while the hole diameter is varied to achieve a range of porosities. The specific diameters employed are 0.904, 1.279, 1.568, 1.809, and 2.022 mm, corresponding to porosities of 0.1, 0.2, 0.3, 0.4, and 0.5, respectively. The geometrical configurations for this design series are presented in Fig. 6 (b).

5.2. Effect of porosity on thermal-hydraulic performance

Given that Design 1 and Design 2 cover an identical porosity range (0.1–0.5), their results are analysed jointly to elucidate the effect of porosity on flow and heat transfer characteristics. This section presents the numerical analysis of the thermal-hydraulic performance of the DPHE equipped with the perforated fins (Design 1 and Design 2). The discussion encompasses the analysis of flow field characteristics, temperature distribution, heat transfer enhancement, Δp, f, and the evaluation of PEC under different geometric parameters. The detailed numerical results of the $\overline{Nu}$, Δp, f, and PEC for the DPHE with annular perforated fins of various design parameters are provided in the "Appendix A" for reference and comparison.

5.2.1. Flow field characteristics

To better understand the effect of the perforated fin structure on the flow and heat transfer characteristics, the flow and temperature field around a full fin are first examined, as shown in Fig. 7. As the fins are arranged periodically along the flow direction, the flow structures induced by each fin exhibit similar distribution characteristics. Compared to the characteristic scale of the vortex structures near the fins, the fin spacing of 200 mm is relatively large. After passing through

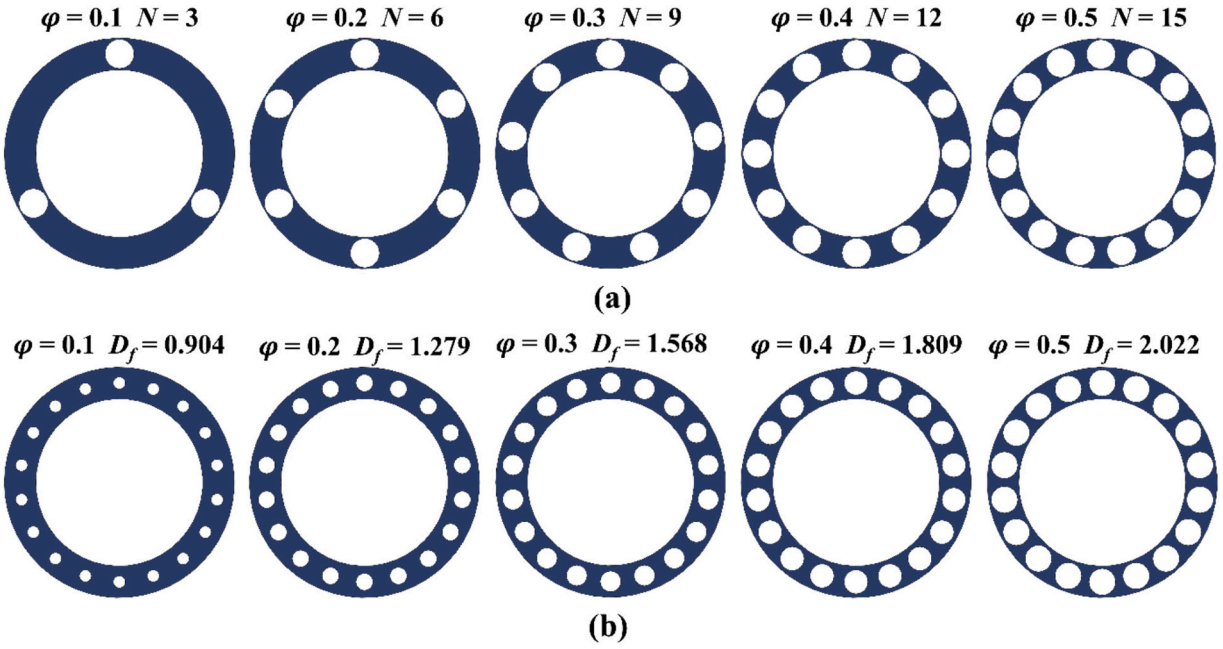

Fig. 6. Schematic diagram of perforated fins: (a) porosity controlled by the hole number, and (b) porosity controlled by the hole diameter.

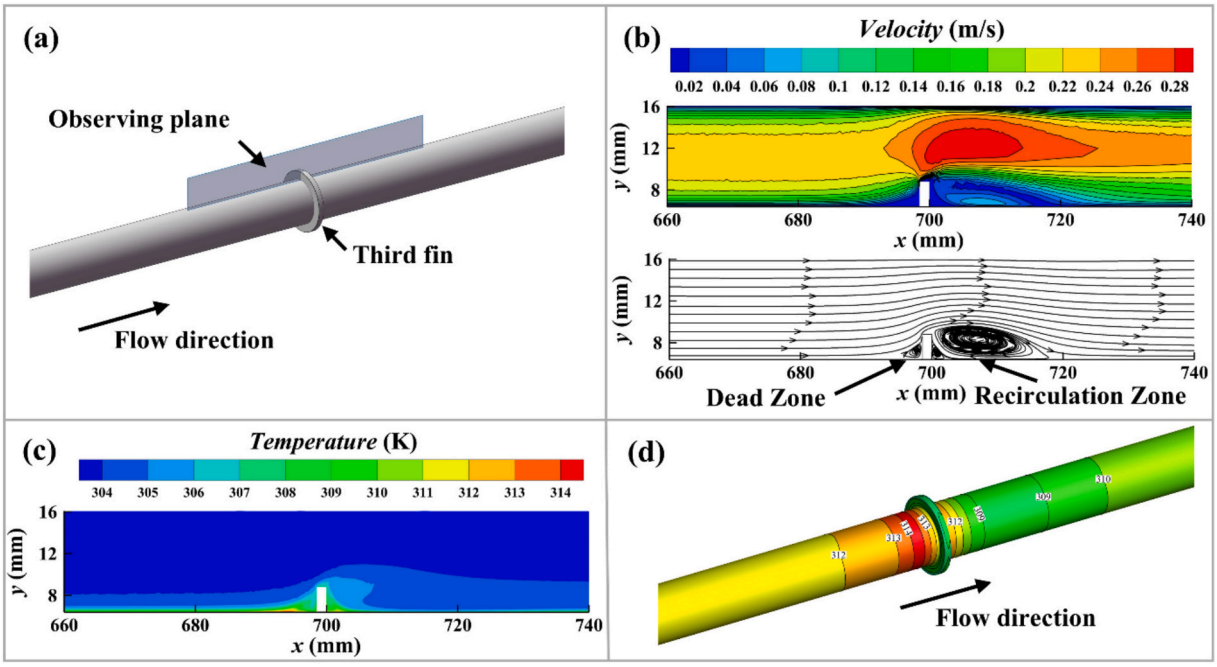

Fig. 7. Flow and temperature field characteristics around a full fin: (a) observation plane setup, (b) velocity and streamline distribution, (c) temperature contour on the observation plane, and (d) temperature distribution on the heat exchange surface.

the fins, the incoming flow generates significant disturbances in the near-wall region and induces local vortex structures. As the flow continues to develop in the axial direction, these near-wall disturbances are gradually smoothed out by the core flow, and the flow structure is re-established before reaching the next fin. Consequently, the upstream and downstream interference between adjacent fins is relatively limited. As a result, this study selected the third fin as a representative location and conducted a detailed analysis of the flow structure in its vicinity. Fig. 7(a) provides the selected observation region located at the third fin, where an observation plane is defined to analyse the local flow behaviour.

Fig. 7(b) presents the velocity contour and streamline distribution on this plane. When the incoming flow encounters the fin, the portion of the flow is blocked by the fin, forming a small recirculation region upstream of the fin. This region behaves as a flow dead zone, in which the local velocity is nearly stagnant, and heat cannot be effectively removed. In contrast, the flow separates after passing over the fin tip, forming a larger recirculation region downstream. Transverse vortices can be observed within this region. These vortices promote mixing between the hot fluid near the wall and the colder fluid in the core flow, and lead to a thinning of the local thermal boundary layer, resulting in a higher wall temperature gradient in the reattachment region. In addition, although

transverse vortices extend the effective residence time of the fluid within the heated region, the local reverse flow and the associated kinetic energy dissipation increase flow resistance, resulting in a higher overall pressure drop.

Fig. 7(c) displays the temperature contour on the same observation plane. A distinct high-temperature zone appears in front of the fin due to the presence of the dead zone. Downstream of the fin, the recirculation and vortex structures facilitate mixing between the warm near-wall fluid and the cooler core flow, resulting in lower wall temperatures compared with the region in front of the fin. This temperature distribution is more clearly illustrated in Fig. 7(d), which presents the temperature contour of the heat exchange surface near the third fin. A distinct high-temperature zone is formed upstream of the fin due to flow obstruction, while a low-temperature zone appears downstream because of the recirculation and enhanced mixing behind the fin.

To further investigate the effect of the perforated structure on the flow field, perforated fin configuration from Design 2 is also analysed. In this design, the number of holes is fixed at 18, while porosity increases with hole diameter. Adopting the same observation plane as in Figs. 7 (a), 8 presents velocity contours near the perforated fins at different porosities and $Re = 4540$. As shown in this figure, perforations allow part of the incoming flow to pass through the holes, forming small jet streams through the fin. As porosity increases, the obstruction effect imposed by the fin on the main flow weakens. Consequently, both the dead zone upstream of the fin and the recirculation zone downstream diminish progressively. At $\varphi > 0.3$, the recirculation region and transverse vortices become significantly weakened, resulting in reduced heat transfer enhancement. Meanwhile, increasing perforation size reduces flow blockage around the fin and decreases the Δp across the channel. A similar flow-evolution pattern can be inferred for Design 1.

A y-z observation plane is placed 5 mm downstream of the third fin. Fig. 9 shows the cross-sectional velocity contours for both Designs 1 and 2 at $Re = 4540$. As shown in Fig. 9(a), the post-perforation jets produce near-wall regions with velocities noticeably higher than those of the adjacent solid-wall sectors. As the hole number and porosity increase, the near-wall velocity behind the fin rises, whereas the core-region velocity decreases. The same trend is provided in Fig. 9(b) for Design 2. The perforations increase the velocity of the flow downstream of the holes, creating a strong velocity gradient in the y-z plane. This velocity gradient drives secondary flow in y-z planes and generates longitudinal vortices along the flow direction.

To more clearly identify the longitudinal vortices induced by the perforation structure, Figs. 10 and 11 presents the x vorticity contours and streamlines of Designs 1 and 2 under different porosities. Since the main flow direction is along the x-axis, the rotation axis of the longitudinal vortices is aligned with the same direction. Therefore, the x-component of vorticity can be used to characterize the rotational strength of the fluid motion in the y-z plane, i.e., the intensity of the longitudinal vortices.

It can be seen from Figs. 10 and 11 that no significant vorticity is observed in the case of the full fin, confirming that streamwise vortices do not form in the absence of perforations. This clearly demonstrates that the vortical structures are entirely induced by the perforations. Longitudinal vortices induced by the perforated fins exist in the counter-rotating vortex pairs, corresponding to the red and blue areas in Fig. 10, and their opposite rotation directions can be observed in Fig. 11. Additionally, excessive porosity is found to be unfavourable for the generation of longitudinal vortices. For both Design 1 and Design 2, when the porosity exceeds 0.3, the vorticity intensity decreases significantly. Under low porosity conditions, the differences in vortex structures induced by different design strategies are more evident. For Design 1, relatively large-scale longitudinal vortices can be observed at $\varphi = 0.1$ and 0.2. Longitudinal vortices continuously induce fluid mixing between the core flow and the near-wall region, disrupting the development of the thermal boundary layer and preventing its stable growth along the flow direction. Meanwhile, near-wall flow disturbance intensifies the velocity gradients near the wall, leading to pronounced vorticity intensity at the thermal interface. By contrast, the strategy of a larger number of smaller sizes in Design 2 leads to the generation of a greater number of smaller-scale longitudinal vortices. Although these small-scale vortices also promote fluid mixing, they are mainly distributed away from the heat transfer surface. Consequently, their effect on disrupting the near-wall boundary layer is limited, resulting in a relatively weaker enhancement of heat transfer. This difference in vortex structure also explains the higher $\overline{Nu}$ observed in Design 1 compared to Design 2 at the same φ, as will be shown in Section 5.2.2.

5.2.2. Heat transfer performance

In this section, the thermal performance of the DPHE is evaluated primarily in terms of the $\overline{Nu}$, which reflects the convective heat transfer capability of the system. This parameter provides a reliable measure for assessing the influence of geometric modifications and operating con-

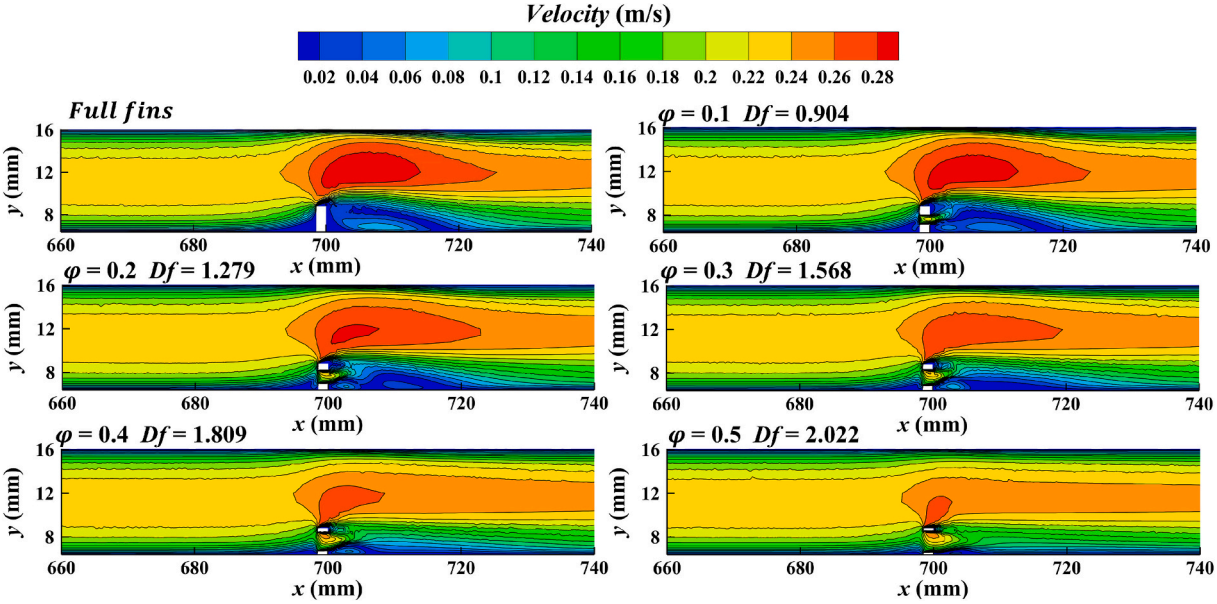

Fig. 8. Velocity contours near perforated fins at different φ (Design 2).

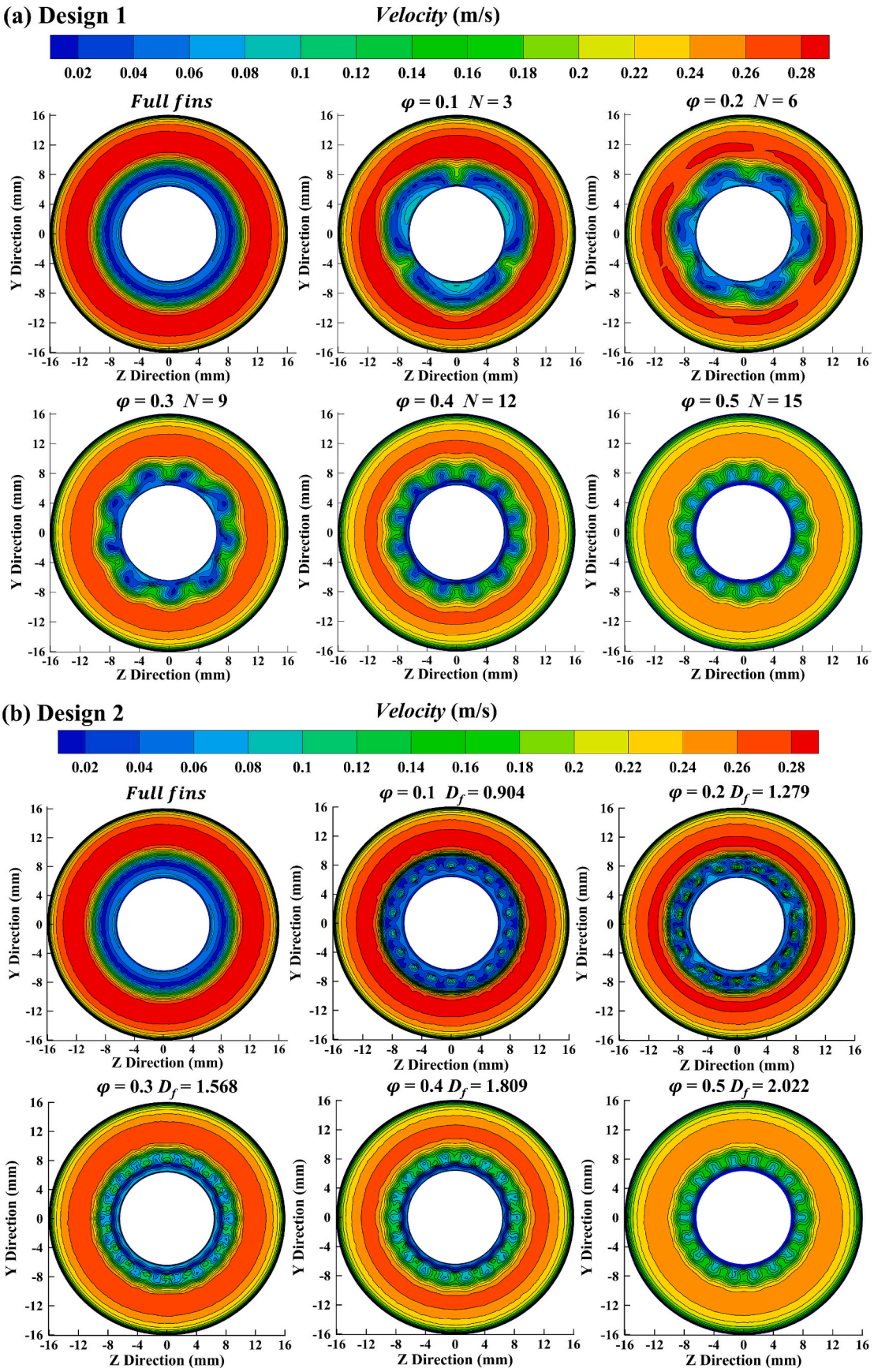

Fig. 9. Cross-sectional velocity contours for (a) Design 1 and (b) Design 2.

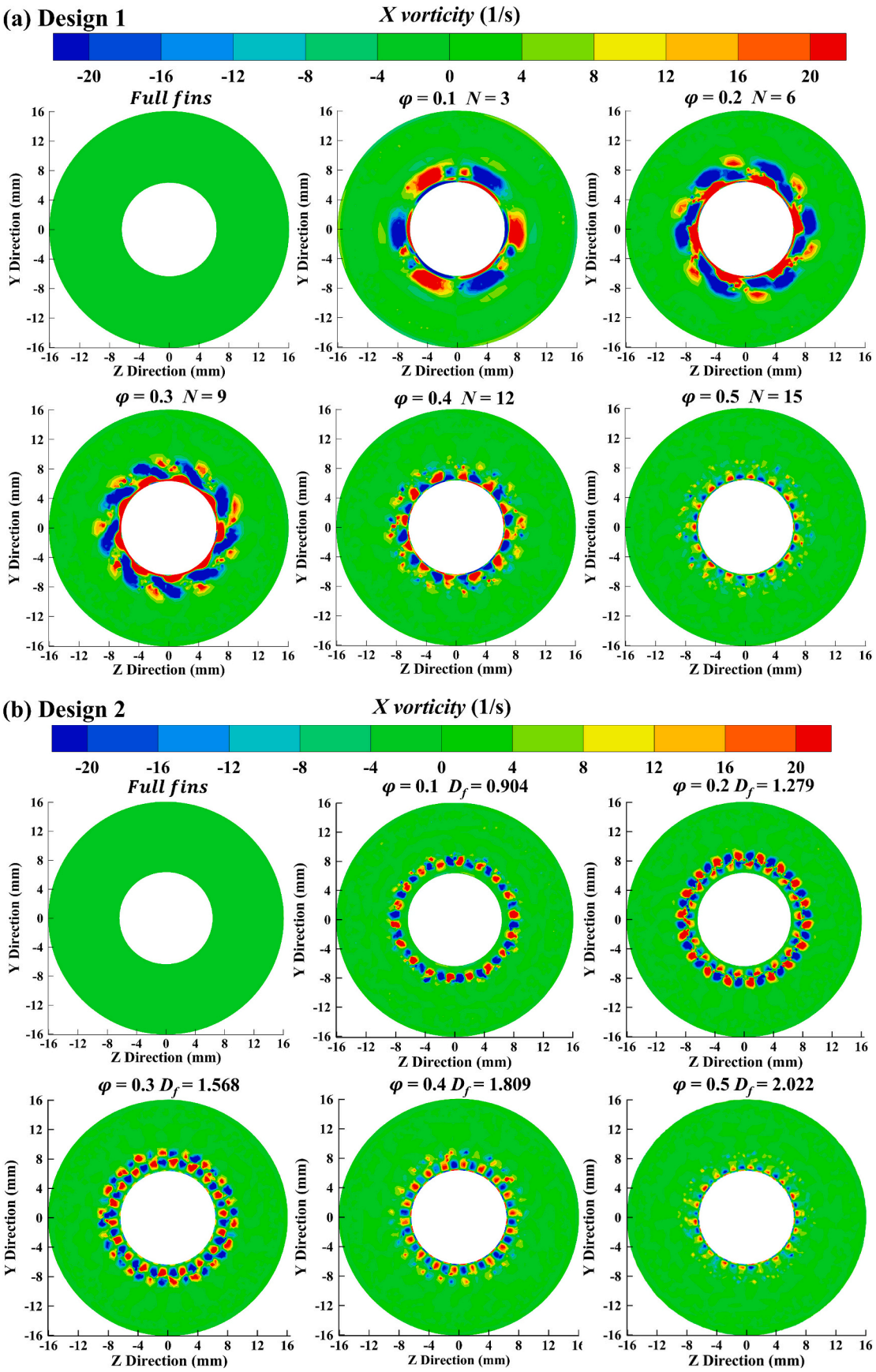

Fig. 10. Cross-sectional vorticity contours for (a) Design 1 and (b) Design 2.

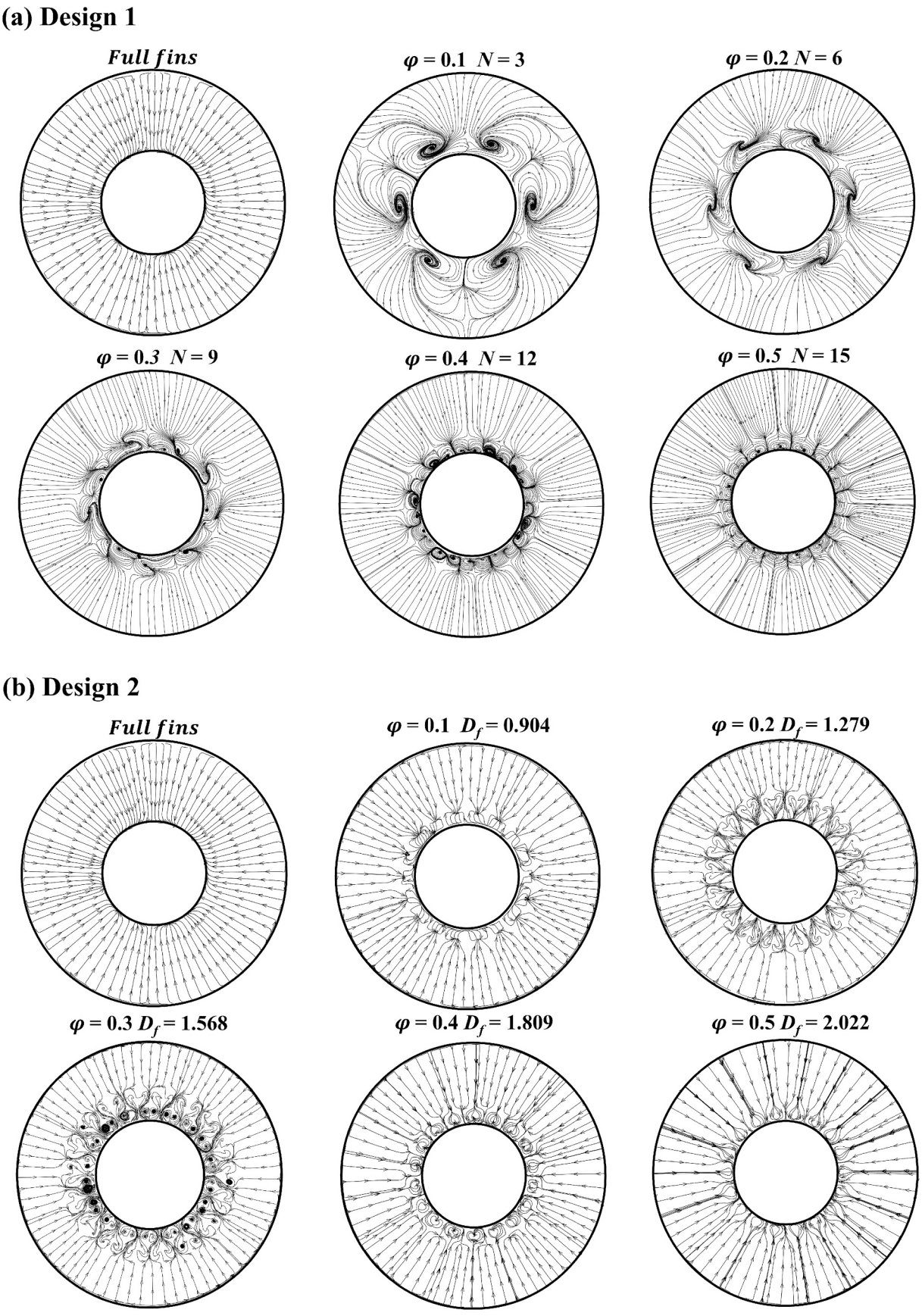

Fig. 11. Streamlines for (a) Design 1 and (b) Design 2.

ditions on the overall heat transfer enhancement, and it has been widely adopted in previous studies to evaluate the performance of various heat exchange configurations [45,52].

Fig. 12 illustrates the variation of the $\overline{Nu}$ with *Re* for Design 1 and Design 2 under different porosities, and the $\overline{Nu}$ increases monotonically with *Re* in all cases. For Design 1, as shown in Fig. 12(a), the $\overline{Nu}$ decreases progressively with increasing porosity and hole number. At $\varphi < 0.2$, the perforated fins show slightly higher $\overline{Nu}$ compared to the full fins, with a maximum value of 124.5 at $\varphi = 0.1$ and $Re = 11{,}350$. This corresponds to improvements of 33.03% and 1.64% over the smooth pipe and full fin, respectively. At low porosity, perforations do not significantly reduce the recirculation region or transverse vortices, while the induced longitudinal vortices enhance fluid mixing and disturbance near the fin, leading to heat transfer enhancement. However, the $\overline{Nu}$ of perforated fins become lower than that of full fins when $\varphi > 0.2$, as the heat transfer enhancement induced by longitudinal vortices is insufficient to compensate for the reduction caused by the weakening of transverse vortices. For Design 2, as shown in Fig. 12(b), the $\overline{Nu}$ also decreases with increasing porosity and hole size. The highest value of $\overline{Nu}$ is calculated around 123.1 at $\varphi = 0.1$ and $Re = 11{,}350$, representing enhancements of 30.87% and 0.52% relative to the smooth tube and full fin, respectively. At the same φ, the $\overline{Nu}$ of Design 2 is consistently lower than that of Design 1. As discussed in Section 5.2.1, this difference can be attributed to the distinct longitudinal vortices induced by the two perforation strategies.

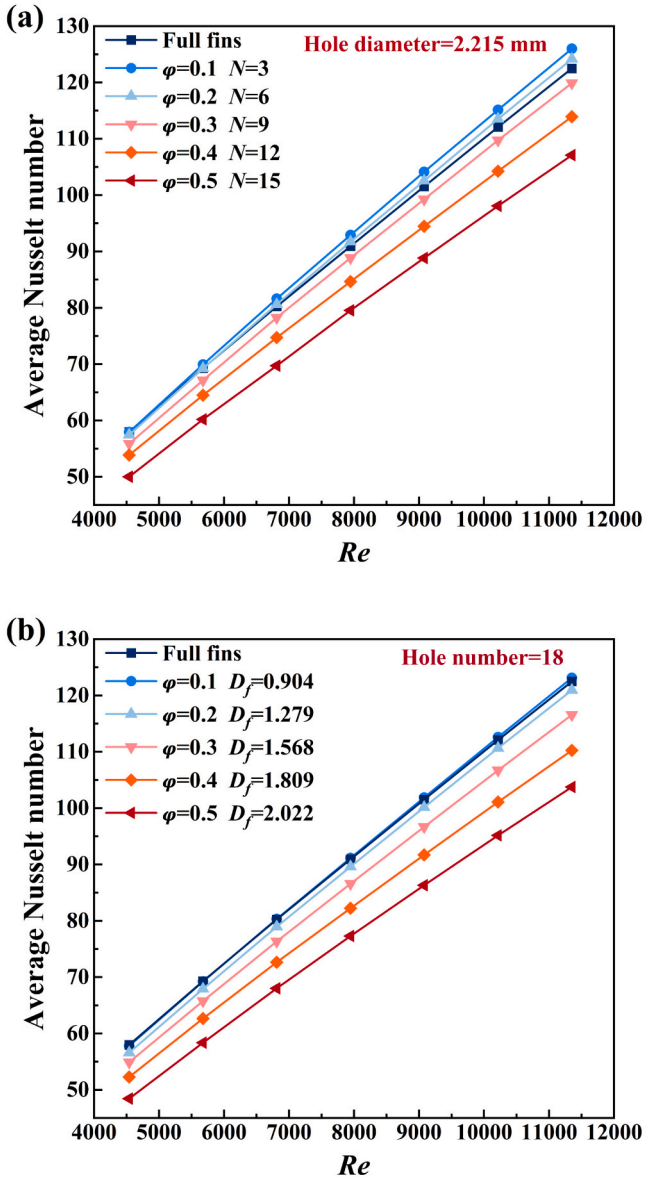

Fig. 12. Variation of $\overline{Nu}$ with *Re* under different φ for (a) Design 1 and (b) Design 2.

Figs. 13 and 14 illustrate the local heat transfer coefficient distribution between the third and fourth fins for Designs 1 and 2 under various porosities. For the full fin configuration, a low heat transfer region appears upstream of the fin due to the dead zone, while a high heat transfer region can be found downstream under the influence of transverse vortices. The locak heat transfer coefficent decreases along the flow direction until the next fin.

Fig. 13 also presents a magnified view of the local heat transfer coefficient near the fin for both the full fin and the perforated fin with $\varphi = 0.1$, as highlighted in regions A and B. Compared with a full fin, the perforated design breaks up the upstream dead zone, significantly improving the low heat transfer region. Local heat transfer coefficients can exceed 4000 W/(m^2·K). Increased porosity causes a gradual weakening of the transverse vortices downstream of the fin, leading to a reduction in the area of high heat transfer. Although the perforations induce longitudinal vortices that enhance the local heat transfer coefficient near the fin, their influence is relatively limited and does not significantly improve overall heat transfer performance. Therefore, the overall heat transfer enhancement remains dominated by transverse vortices. As shown in Fig. 14 for Design 2, the high heat transfer region decreases with increasing porosity. However, at $\varphi = 0.1$, no pronounced high heat transfer region is observed upstream of the fin compared to Design 1, as indicated in region A. In contrast, as the hole size increases, a high heat transfer region can be observed at $\varphi = 0.4$, as highlighted in region B. This indicates that larger perforation sizes are more effective in enhancing local heat transfer.

The relative contributions of longitudinal and transverse vortices to heat transfer enhancement can be distinguished based on the analysis of the $\overline{Nu}$ and local heat transfer coefficient. Overall, annular fins enhance heat transfer primarily through the induction of transverse vortices. Perforations weaken transverse vortices and induce a limited intensity of longitudinal vortices. These longitudinal vortices improve local heat transfer near the fin, but their contribution remains secondary. The overall heat transfer enhancement is still dominated by transverse vortices, as evidenced by the decrease in both the $\overline{Nu}$ and the local heat transfer coefficient with increasing porosity due to the weakening of transverse vortices.

5.2.3. *Pressure drop and flow resistance*

In this study, the pressure drop is defined as the static pressure difference between the inlet and outlet cross-sections of the test section. As the computational domain encompasses the perforated fins and the associated flow disturbances, the resulting pressure drop incorporates both frictional and minor losses caused by the fin structures. This definition aligns with standard experimental measurements, which involve measuring the pressure difference between two pressure taps positioned at the inlet and outlet of the test section [45]. Fig. 15 presents the variation of the Δp coefficient with *Re* for different porosities with the range of 4540–11,350. For both Design 1 and Design 2, the Δp decreases consistently with increasing porosity. Perforations reduce flow resistance by weakening the blockage effect of the fin surface and allowing fluid to pass through the holes. Larger hole diameters and fewer holes are more effective in reducing Δp when the porosities are the same. In addition, for both designs, the maximum Δp reduction occurs at the highest porosity of 0.5, with a decrease of up to 22.03% for Design 1 and 20.57% for Design 2 compared with the full fin case at a *Re* of 11,350.

A similar trend and difference can be observed in the *f*, as shown in Fig. 16. Although the *f* decreases with increasing porosity for Design 1 and Design 2, small deviations appear between different fin

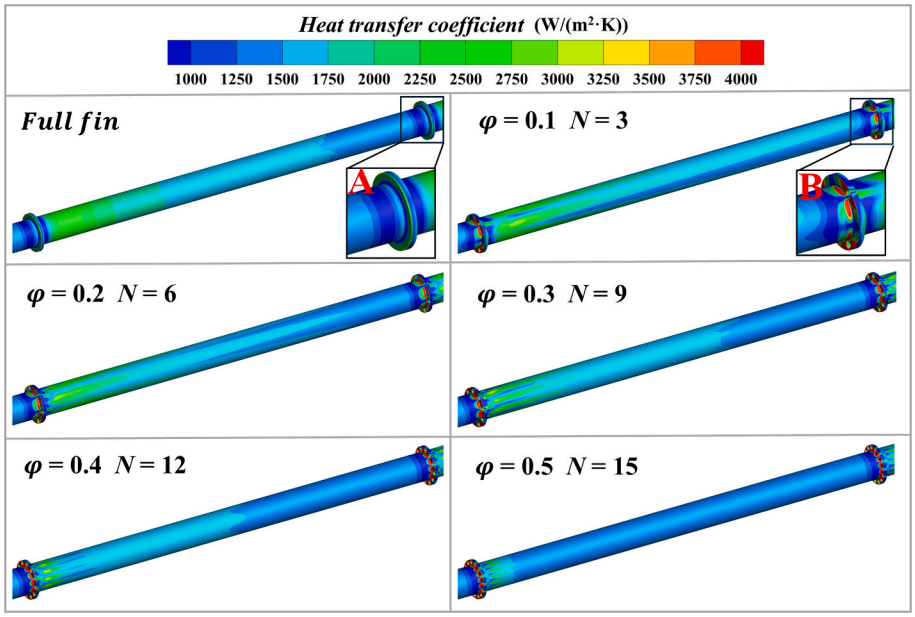

Fig. 13. Local heat transfer coefficient distribution between the third and fourth fins for Design 1 under different porosities.

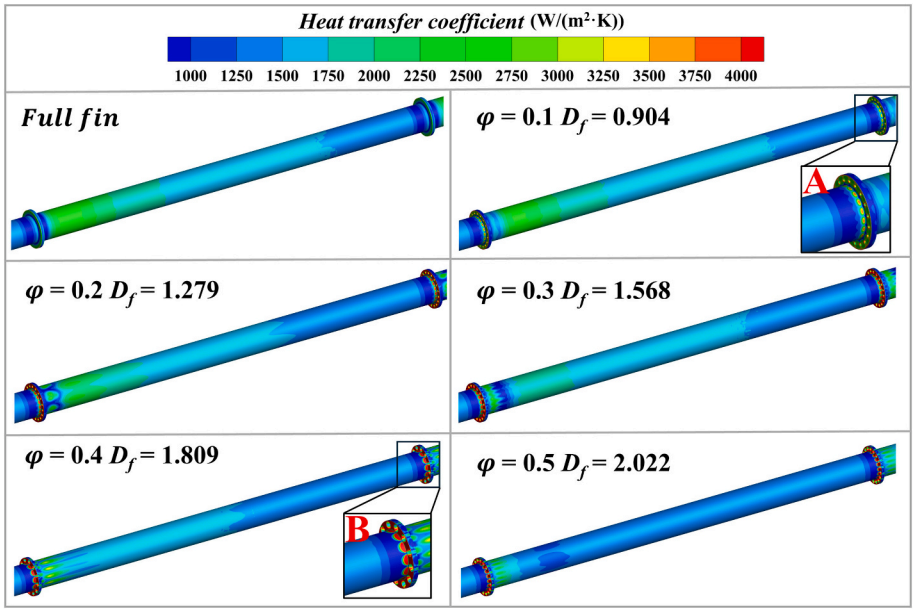

Fig. 14. Local heat transfer coefficient distribution between the third and fourth fins for Design 2 under different porosities.

configurations at the same porosity level. This finding indicates that, while the overall porosity dominates the variation of Δp and f, the detailed design strategy can further influence the flow resistance characteristics. These effects are discussed in greater detail in the following sections. Furthermore, as the *Re* increases, the absolute Δp rises due to higher flow velocity, but the f decreases because it is normalized by the square of the velocity.

5.2.4. Performance evaluation criterion analysis

To evaluate the overall thermal performance, the performance evaluation criterion is adopted to assess the balance between heat transfer enhancement and flow resistance. Fig. 17 presents the variation of *PEC* with porosity for both Design 1 and Design 2 across different *Re*. In all cases, the *PEC* values are greater than 1, indicating that all perforated fin configurations provide better overall thermal performance compared with the smooth pipe. When the φ is controlled by the number of holes (Design 1), the *PEC* first increases and then decreases with increasing porosity, as shown in Fig. 17(a). The highest *PEC* value is obtained at a porosity of 0.2. At the same φ, the *PEC* decreases slightly as the *Re* increases. The maximum *PEC* of 1.186 is achieved at $\varphi = 0.2$ and $Re = 4540$. In addition, the largest improvement in *PEC* compared with the full fin configurations occurs at $Re = 11{,}350$ and $\varphi = 0.2$, where the *PEC* of the perforated fin and the full fin are 1.153 and 1.092, respectively. Overall, when $\varphi \leq 0.2$, the *PEC* values of perforated configurations are consistently higher than those of the full fin configuration. However, when $\varphi > 0.2$, the *PEC* decreases below that of the full fin. This indicates that, although pumping power decreases at higher φ, the reduction in heat transfer enhancement outweighs this benefit, leading to a decrease in overall thermal performance.

When the porosity is controlled by the hole diameter (Design 2), a

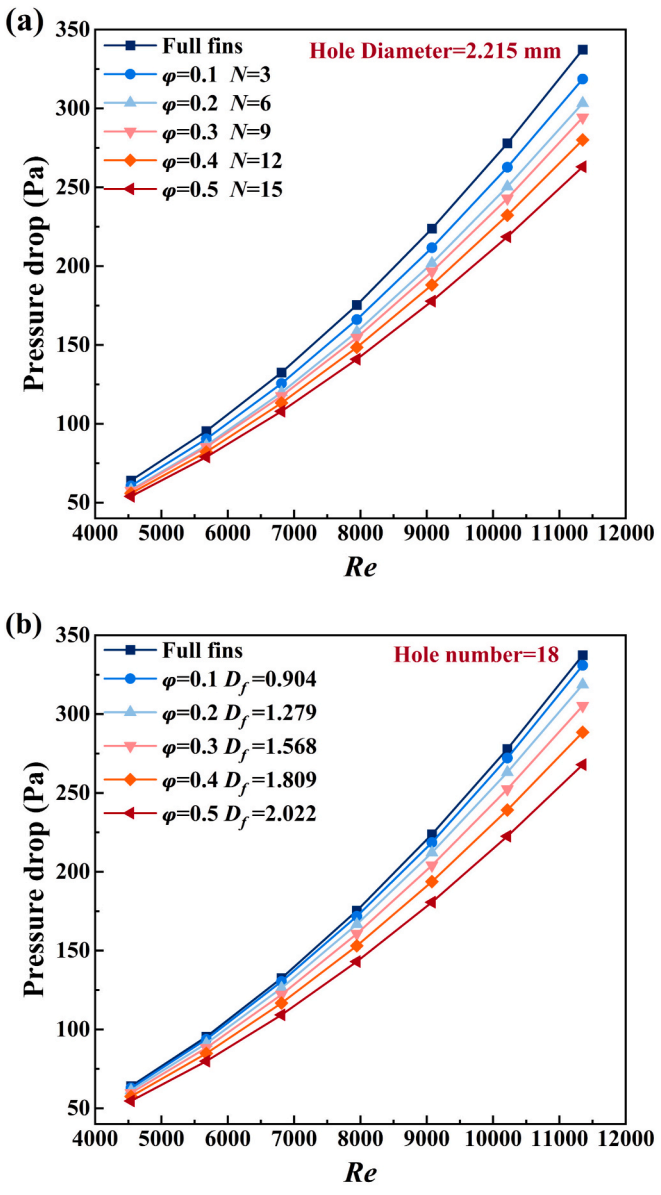

Fig. 15. Variation of Δp with Re under different φ for (a) Design 1 and (b) Design 2.

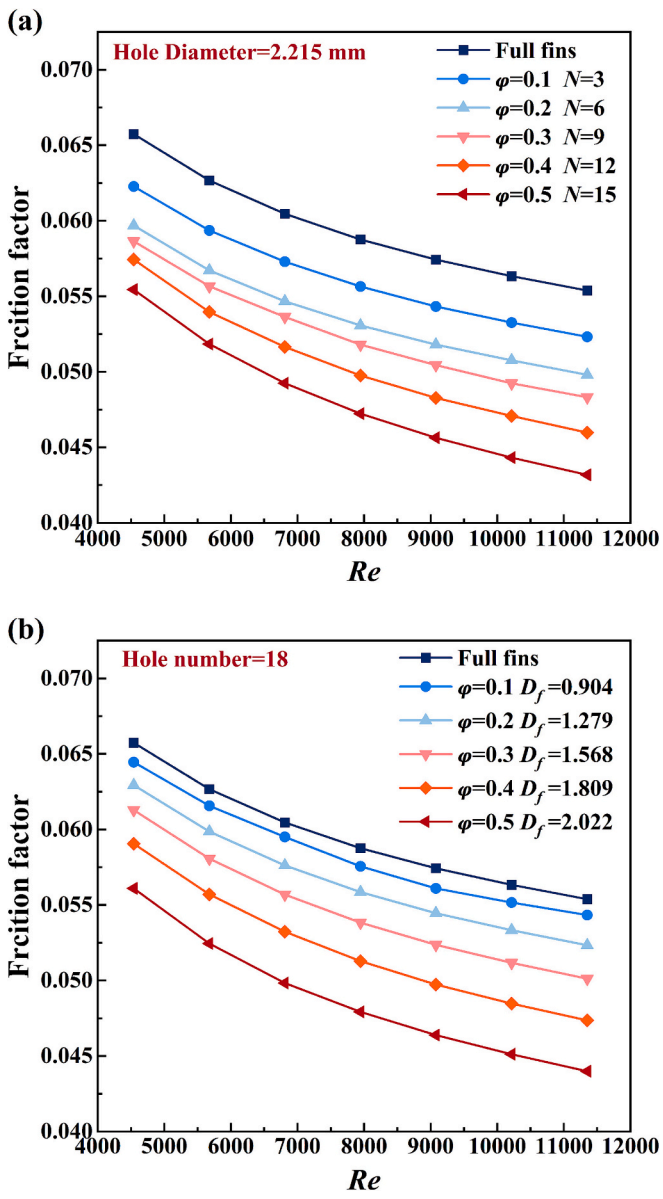

Fig. 16. Variation of f with Re under different φ for (a) Design 1 and (b) Design 2.

similar trend is observed, as shown in Fig. 17(b). The optimal *PEC* occurs at a porosity of 0.1, where the values range from 1.103 to 1.163. Although the *PEC* is slightly higher than that of the full fin configuration, the improvement is not significant. When porosity exceeds 0.1, the *PEC* gradually decreases, and at $\varphi = 0.3$, 0.4, and 0.5, the *PEC* becomes even lower than that of the full fin. By comparing the two perforation strategies, it can be concluded that controlling porosity by hole number (Design 1) results in consistently higher *PEC* values than controlling it by hole diameter (Design 2) under the same φ and Re. In conclusion, within the specific geometric configuration, the range of Re, and thermal boundary conditions considered in the present study, a porosity of 0.2 provides the best balance between heat transfer enhancement and Δp. Although Design 2 achieved its highest *PEC* at a porosity of 0.1, its absolute value is lower than that of Design 1. It should be noted that the observed PEC improvement is primarily attributed to the reduction in flow resistance, while the contribution of perforations to heat transfer enhancement remains limited. From an engineering perspective, the decrease in flow resistance implies a lower pumping power requirement, contributing to potential energy savings in practical DPHE systems. Therefore, the PEC enhancement in this study should be interpreted as an improvement in flow efficiency rather than a significant increase in heat transfer performance.

5.3. *Effect of hole number and diameter at constant porosity*

5.3.1. *Design 3*

As discussed in the previous sections, although the variations of *Nu*, Δp, *f*, and *PEC* with *Re* and porosity exhibit consistent overall trends across different perforation designs, slight differences are still observed at the same porosity. To further examine this difference, the porosity is fixed at 0.2, which is identified as the overall optimum in the preceding analysis. In Design 3, both the hole number and the hole diameter are varied simultaneously while maintaining a constant porosity of 0.2, as shown in Fig. 18. This configuration ensures that the total perforated area of the fins remains unchanged, so that the influence of hole geometry can be studied independently of porosity. This section aims to clarify the respective influences of hole number and diameter on flow characteristics and heat transfer enhancement under an identical

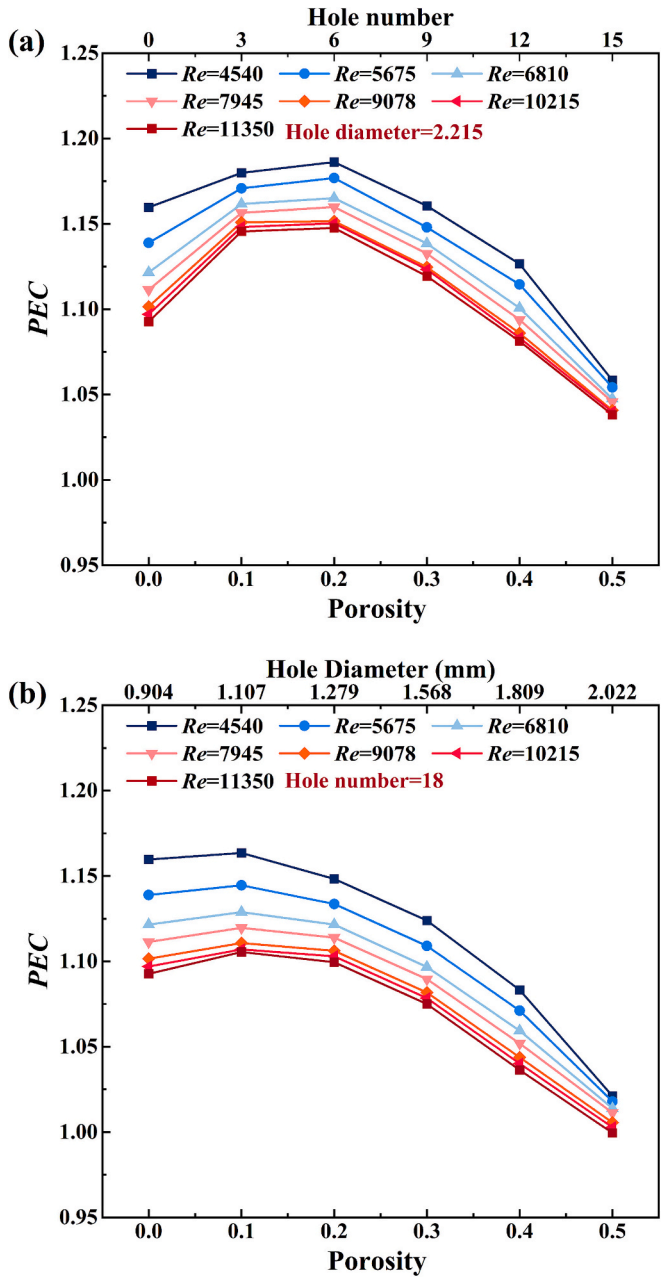

Fig. 17. Variation of *PEC* with φ for (a) Design 1 and (b) Design 2.

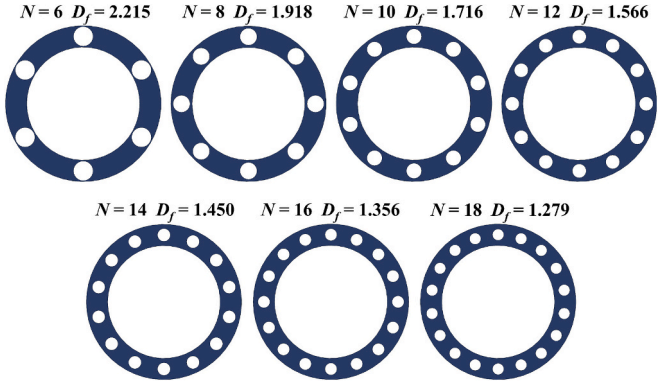

Fig. 18. Fin geometries for Design 3, showing different combinations of hole number and hole diameter at $\varphi = 0.2$.

porosity condition.

5.3.2. Heat transfer performance

Fig. 19 presents the variation of the $\overline{Nu}$ with hole number and hole diameter under $\varphi = 0.2$. The changes in the $\overline{Nu}$ caused by variations in hole number and diameter are relatively small, indicating that porosity plays the dominant role in determining the heat transfer enhancement rather than hole number and hole diameter. With increasing hole numbers, the average $\overline{Nu}$ shows a slight downward trend. The maximum reduction of approximately 3.15% is observed between the cases of $N = 6$ ($D_f = 2.215$ mm) and $N = 18$ ($D_f = 1.279$ mm) at $Re = 11{,}350$, where the corresponding $\overline{Nu}$ are 124.77 and 120.95, respectively.

5.3.3. Pressure drop and flow resistance

Fig. 20 illustrates the variations of (a) Δp and (b) f with hole number and hole diameter under a constant porosity of 0.2. In Fig. 20(a), the Δp increases slightly with the increasing hole number and decreasing hole diameter. Because of the relatively large range of the y-axis, this variation appears less clear visually. At $Re = 4540$, the Δp for the configurations with $N = 6$ ($D_f = 2.215$ mm) and $N = 18$ ($D_f = 1.279$ mm) are 58.17 Pa and 61.33 Pa, respectively, representing an increase of approximately 5.16%. In Fig. 20(b), the f shows a more distinct increasing trend as the hole number increases and the hole diameter decreases. It can be concluded from these results that under a constant total flow area, using more holes and a smaller diameter increases the total lateral surface area of the perforation channels, enlarging the wall contact area and intensifying wall shear and viscous losses. As a result, both the Δp and the f become higher for configurations with more holes and smaller diameters.

5.3.4. Performance evaluation criterion analysis

Fig. 21 presents the variation of the *PEC* for different configurations in Design 3 with varying hole numbers and hole diameters. The *PEC* decreases gradually with increasing hole number and decreasing hole diameter. Configurations with fewer and larger holes yield higher *PEC* values, as they maintain better heat transfer performance while inducing lower Δp. In addition, as the *Re* increases, the *PEC* decreases in all configurations of hole numbers and hole diameters. The decrease in *PEC* with increasing *Re* can be attributed to the fact that, at higher flow rates,

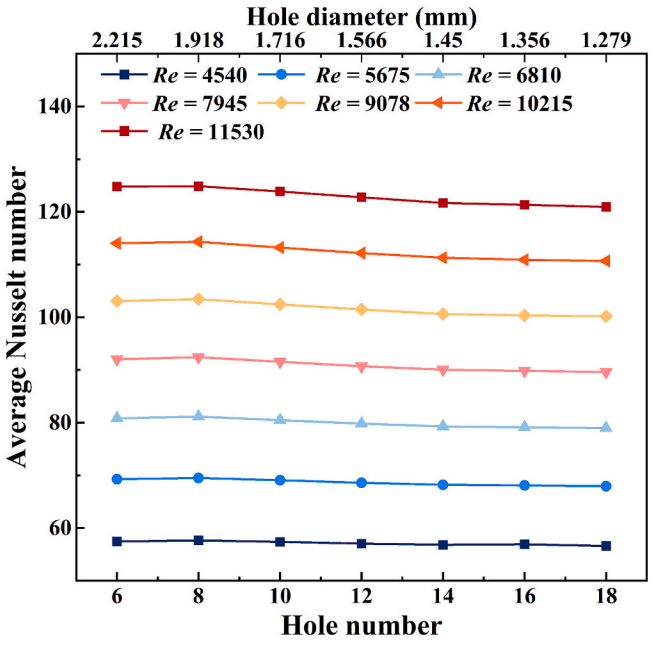

Fig. 19. Variation of the $\overline{Nu}$ with hole number and hole diameter for Design 3.

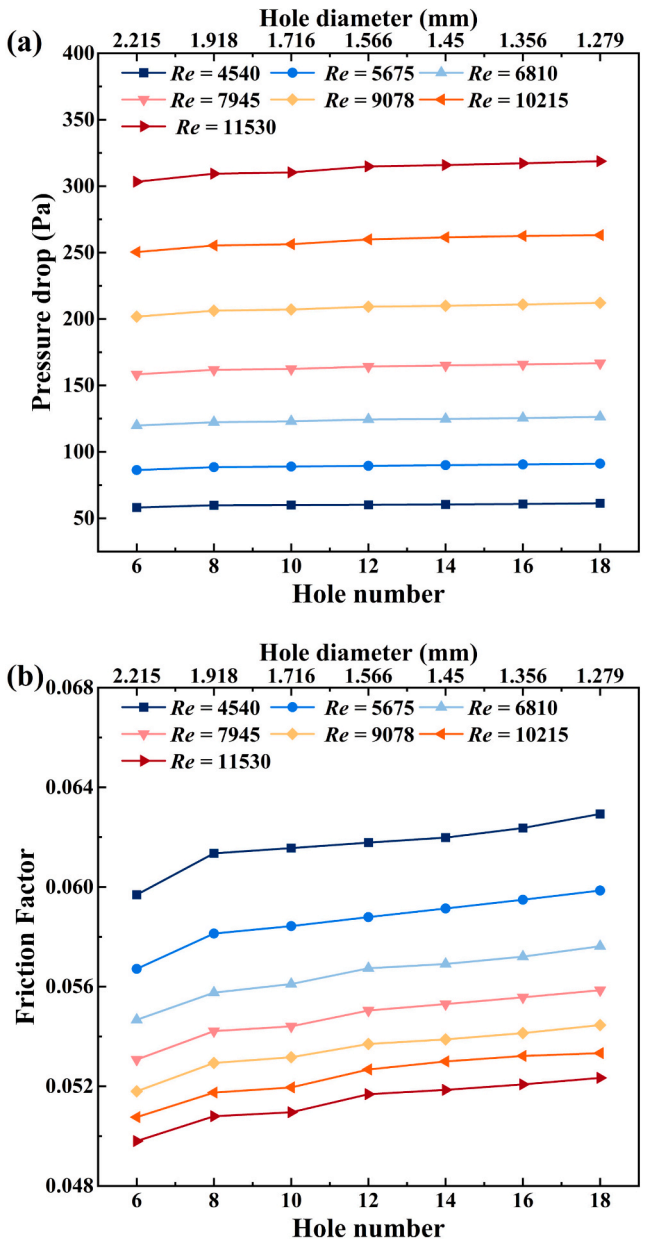

Fig. 20. Variation of Δp and f with hole number and hole diameter for Design 3.

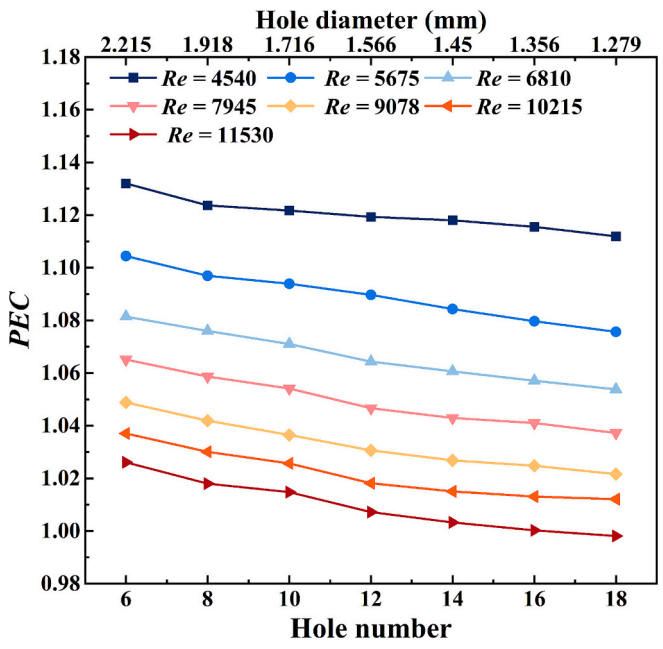

Fig. 21. Variation of *PEC* with hole number and hole diameter for Design 3.

the Δp rises more sharply than the heat transfer enhancement. Consequently, the overall thermal-hydraulic performance becomes less favourable despite the improvement in convective heat transfer. For instance, at $\varphi = 0.2$, the maximum *PEC* of 1.186 is obtained at $Re = 4540$.

5.4. Generalizability and applicability of the results

The present study establishes a perforation design strategy based on the analysis of perforated annular fins. The proposed strategy and the associated trends are expected to apply to other heat transfer enhancement devices that rely on similar flow mechanisms, including radial fins, circular-ring vortex generators, and rib structures. However, the applicability of the proposed strategy to configurations governed by different mechanisms remains to be further investigated.

Distilled water is used as the working fluid in this study, and the effects of fluids with significantly different Prandtl numbers are not explicitly examined. However, the enhancement mechanism identified in this study is primarily associated with flow structure modification. Therefore, the qualitative trends are expected to remain valid for fluids with different Prandtl numbers [53]. It should be noted that the Prandtl number affects the relative thickness of the thermal boundary layer and the thermal diffusion characteristics, influencing heat transfer enhancement and flow resistance. Consequently, the quantitative performance may vary for different thermal fluids [54]. In addition, the *Re* range considered in this study is limited to 4540–11,350. As the *Re* increases, the flow structure and turbulence characteristics may change, influencing heat transfer and flow behaviours. Therefore, the conclusions of this study may not be directly extrapolated to significantly higher *Re*.

All simulations are completed under fixed fin thickness, spacing, and height. Based on the considered geometric parameters and operating conditions, an optimal porosity of approximately 0.2 is identified. However, this optimal value is not universal, as it depends on the geometric parameter. Therefore, for different geometric configurations or operating conditions, the optimal porosity should be re-determined. In addition, a uniform heat flux boundary condition is adopted. The present study does not consider the thermal coupling between the hot and cold fluids and the axial redistribution of wall heat flux. Therefore, the conclusions in this study should be interpreted as relative design guidance under the specified thermal boundary condition, rather than as precise predictions of absolute performance in practical DPHE operations. Furthermore, the present study does not explicitly examine the effects of different heat flux levels. Variations in heat flux will influence the bulk and thermal interface temperature, fluid properties, and the development of the thermal boundary layer, affecting the quantitative values of heat transfer and flow resistance. Consequently, although the overall trends are expected to remain qualitatively consistent, the optimal porosity may exhibit slight variations under different heat flux conditions.

6. Conclusion

A comprehensive numerical investigation of a DPHE with perforated annular fins has been conducted to evaluate the effects of perforated fin geometry on flow and heat transfer performance using a three-fold strategy. Several conclusions can be drawn from this study as follows:

1. The perforated structure alters the internal flow field and disrupts the upstream dead zone observed in full-fin configurations. The induced longitudinal vortices enhance local heat transfer near the fin, while the perforations provide additional flow paths that reduce flow resistance and Δp.
2. The longitudinal vortices induced by the perforations make a limited contribution to overall heat transfer enhancement, while the transverse vortices provide the dominant contribution. Excessive porosity weakens the recirculation zone and transverse vortex, leading to a deterioration in heat transfer performance.
3. At a constant porosity, the thermal-hydraulic performance is relatively insensitive to variations in hole number and hole size. This suggests that porosity plays a dominant role in determining heat transfer and pressure drop characteristics. Consequently, porosity should be prioritized in the design of perforated annular fins, with other geometric parameters further optimized.
4. Configurations with larger hole diameters and fewer perforations are more effective for heat transfer enhancement at a constant porosity. The highest $\overline{Nu}$ of 126.0 is observed for the case with $\varphi = 0.1$, $D_f = 2.215$ mm, $N = 3$ and $Re = 11{,}350$. A porosity of 0.2 exhibits the best thermal-hydraulic performance, with a maximum PEC of 1.186 observed at $\varphi = 0.2$, $D_f = 2.215$ mm, $N = 6$, and $Re = 4540$.

CRediT authorship contribution statement

Zhihang Yan: Writing – original draft, Visualization, Validation, Software, Methodology, Data curation. **Hiwa Najafi:** Writing – review & editing, Validation, Investigation, Formal analysis. **Jong Boon Ooi:** Writing – review & editing, Supervision. **Boon Thong Tan:** Writing – review & editing, Supervision. **Foo Wah Low:** Writing – review & editing, Supervision. **James Ren:** Writing – review & editing, Supervision, Funding acquisition. **Cheen Sean Oon:** Writing – review & editing, Supervision, Resources, Methodology, Investigation, Funding acquisition.

Declaration of competing interest

The authors declare that they have no known competing financial interests or personal relationships that could have appeared to influence the work reported in this paper.

Acknowledgements

The work received support from the European Union's Horizon 2020 research and innovation programme under the Marie Skłodowska-Curie grant agreement No. 101130406, and the UKRI Engineering and Physical Sciences Research Council No. EP/Y03659X/1.

Appendix A

The annulus-side average Nusselt number ($\overline{Nu}$), pressure drop (Δp), friction factor (f), and Performance evaluation criterion (PEC) of double-pipe heat exchangers equipped with perforated fins of varying hole numbers, hole diameters, and porosities.

Number	Re	N	D_f (mm)	φ	$\overline{Nu}$	Δp	f	PEC
1	4540.34	No fins	No fins	No fins	43.967	43.526	0.045	1
2	5675.21	No fins	No fins	No fins	52.820	62.451	0.041	1
3	6810.52	No fins	No fins	No fins	61.479	84.126	0.038	1
4	7945.55	No fins	No fins	No fins	69.693	108.387	0.036	1
5	9078.43	No fins	No fins	No fins	77.917	135.185	0.035	1
6	10,215.79	No fins	No fins	No fins	85.826	164.695	0.033	1
7	11,350.76	No fins	No fins	No fins	93.593	196.317	0.032	1
8	4540.34	Full fins	Full fins	Full fins	57.996	64.066	0.066	1.160
9	5675.21	Full fins	Full fins	Full fins	69.287	95.418	0.063	1.139
10	6810.52	Full fins	Full fins	Full fins	80.242	132.585	0.060	1.122
11	7945.55	Full fins	Full fins	Full fins	90.932	175.374	0.059	1.111
12	9078.43	Full fins	Full fins	Full fins	101.530	223.765	0.057	1.102
13	10,215.79	Full fins	Full fins	Full fins	112.090	277.918	0.056	1.097
14	11,350.76	Full fins	Full fins	Full fins	122.492	337.349	0.055	1.093
15	4540.34	3	2.215	0.1	57.603	60.691	0.062	1.173
16	5675.21	3	2.215	0.1	69.323	90.388	0.059	1.160
17	6810.52	3	2.215	0.1	80.785	125.624	0.057	1.150
18	7945.55	3	2.215	0.1	91.917	166.097	0.056	1.144
19	9078.43	3	2.215	0.1	102.908	211.680	0.054	1.137
20	10,215.79	3	2.215	0.1	113.778	262.761	0.053	1.135
21	11,350.76	3	2.215	0.1	124.507	318.690	0.052	1.132
22	4540.34	6	2.215	0.2	57.446	58.170	0.060	1.186
23	5675.21	6	2.215	0.2	69.252	86.354	0.057	1.177
24	6810.52	6	2.215	0.2	80.603	119.879	0.055	1.165
25	7945.55	6	2.215	0.2	91.733	158.400	0.053	1.160
26	9078.43	6	2.215	0.2	102.551	201.823	0.052	1.152
27	10,215.79	6	2.215	0.2	113.530	250.440	0.051	1.150
28	11,350.76	6	2.215	0.2	124.169	303.331	0.050	1.148
29	4540.34	9	2.215	0.3	55.871	57.540	0.059	1.161
30	5675.21	9	2.215	0.3	67.134	85.263	0.056	1.148
31	6810.52	9	2.215	0.3	78.262	117.601	0.054	1.138
32	7945.55	9	2.215	0.3	88.854	154.613	0.052	1.133
33	9078.43	9	2.215	0.3	99.274	196.565	0.050	1.125
34	10,215.79	9	2.215	0.3	109.747	242.923	0.049	1.123
35	11,350.76	9	2.215	0.3	119.897	294.288	0.048	1.119
36	4540.34	12	2.215	0.4	53.864	55.978	0.057	1.127
37	5675.21	12	2.215	0.4	64.504	82.159	0.054	1.115

(*continued on next page*)

(*continued*)

Number	*Re*	*N*	D_f (mm)	φ	$\overline{Nu}$	Δp	f	*PEC*
38	6810.52	12	2.215	0.4	74.723	113.262	0.052	1.101
39	7945.55	12	2.215	0.4	84.668	148.508	0.050	1.094
40	9078.43	12	2.215	0.4	94.464	188.090	0.048	1.086
41	10,215.79	12	2.215	0.4	104.261	232.265	0.047	1.083
42	11,350.76	12	2.215	0.4	113.921	280.050	0.046	1.081
43	4540.34	15	2.215	0.5	50.012	54.030	0.055	1.058
44	5675.21	15	2.215	0.5	60.206	78.932	0.052	1.054
45	6810.52	15	2.215	0.5	69.722	107.981	0.049	1.044
46	7945.55	15	2.215	0.5	79.549	140.964	0.047	1.046
47	9078.43	15	2.215	0.5	88.846	177.793	0.046	1.041
48	10,215.79	15	2.215	0.5	98.095	218.670	0.044	1.040
49	11,350.76	15	2.215	0.5	107.112	263.015	0.043	1.038
50	4540.34	18	0.904	0.1	57.811	62.818	0.064	1.164
51	5675.21	18	0.904	0.1	69.222	93.746	0.062	1.145
52	6810.52	18	0.904	0.1	80.336	130.477	0.060	1.129
53	7945.55	18	0.904	0.1	91.152	171.779	0.058	1.122
54	9078.43	18	0.904	0.1	101.886	218.583	0.056	1.114
55	10,215.79	18	0.904	0.1	112.605	272.166	0.055	1.110
56	11,350.76	18	0.904	0.1	123.134	330.938	0.054	1.105
57	4540.34	18	1.279	0.2	56.600	61.333	0.063	1.148
58	5675.21	18	1.279	0.2	67.921	91.144	0.060	1.134
59	6810.52	18	1.279	0.2	78.964	126.345	0.058	1.122
60	7945.55	18	1.279	0.2	89.611	166.702	0.056	1.114
61	9078.43	18	1.279	0.2	100.167	212.183	0.054	1.106
62	10,215.79	18	1.279	0.2	110.661	263.113	0.053	1.103
63	11,350.76	18	1.279	0.2	120.952	318.772	0.052	1.099
64	4540.34	18	1.568	0.3	54.911	59.727	0.061	1.124
65	5675.21	18	1.568	0.3	65.776	88.412	0.058	1.109
66	6810.52	18	1.568	0.3	76.342	122.117	0.056	1.097
67	7945.55	18	1.568	0.3	86.585	160.667	0.054	1.090
68	9078.43	18	1.568	0.3	96.686	204.039	0.052	1.082
69	10,215.79	18	1.568	0.3	106.724	252.462	0.051	1.078
70	11,350.76	18	1.568	0.3	116.564	305.274	0.050	1.075
71	4540.34	18	1.809	0.4	52.275	57.554	0.059	1.083
72	5675.21	18	1.809	0.4	62.657	84.818	0.056	1.071
73	6810.52	18	1.809	0.4	72.642	116.723	0.053	1.059
74	7945.55	18	1.809	0.4	82.246	153.050	0.051	1.052
75	9078.43	18	1.809	0.4	91.698	193.786	0.050	1.044
76	10,215.79	18	1.809	0.4	101.088	239.138	0.048	1.040
77	11,350.76	18	1.809	0.4	110.272	288.484	0.047	1.036
78	4540.34	18	2.022	0.5	48.438	54.671	0.056	1.021
79	5675.21	18	2.022	0.5	58.362	79.863	0.052	1.018
80	6810.52	18	2.022	0.5	68.014	109.265	0.050	1.014
81	7945.55	18	2.022	0.5	77.305	143.033	0.048	1.011
82	9078.43	18	2.022	0.5	86.315	180.746	0.046	1.006
83	10,215.79	18	2.022	0.5	95.159	222.588	0.045	1.003
84	11,350.76	18	2.022	0.5	103.764	267.958	0.044	0.999
85	4540.34	8	1.918	0.2	57.662	59.792	0.061	1.180
86	5675.21	8	1.918	0.2	69.479	88.513	0.058	1.171
87	6810.52	8	1.918	0.2	81.153	122.268	0.056	1.165
88	7945.55	8	1.918	0.2	92.413	161.805	0.054	1.160
89	9078.43	8	1.918	0.2	103.449	206.252	0.053	1.153
90	10,215.79	8	1.918	0.2	114.308	255.320	0.052	1.151
91	11,350.76	8	1.918	0.2	124.867	309.403	0.051	1.146
92	4540.34	10	1.716	0.2	57.376	59.994	0.062	1.173
93	5675.21	10	1.716	0.2	69.062	88.967	0.058	1.162
94	6810.52	10	1.716	0.2	80.462	123.023	0.056	1.153
95	7945.55	10	1.716	0.2	91.552	162.383	0.054	1.148
96	9078.43	10	1.716	0.2	102.433	207.145	0.053	1.140
97	10,215.79	10	1.716	0.2	113.214	256.322	0.052	1.138
98	11,350.76	10	1.716	0.2	123.867	310.368	0.051	1.136
99	4540.34	12	1.566	0.2	57.053	60.212	0.062	1.165
100	5675.21	12	1.566	0.2	68.567	89.520	0.059	1.151
101	6810.52	12	1.566	0.2	79.818	124.412	0.057	1.140
102	7945.55	12	1.566	0.2	90.698	164.273	0.055	1.133
103	9078.43	12	1.566	0.2	101.474	209.234	0.054	1.126
104	10,215.79	12	1.566	0.2	112.171	259.892	0.053	1.123
105	11,350.76	12	1.566	0.2	122.759	314.803	0.052	1.121
106	4540.34	14	1.450	0.2	56.799	60.408	0.062	1.158
107	5675.21	14	1.450	0.2	68.214	90.041	0.059	1.143
108	6810.52	14	1.450	0.2	79.270	124.794	0.057	1.131
109	7945.55	14	1.450	0.2	90.057	165.045	0.055	1.123
110	9078.43	14	1.450	0.2	100.615	209.949	0.054	1.115
111	10,215.79	14	1.450	0.2	111.311	261.480	0.053	1.112
112	11,350.76	14	1.450	0.2	121.684	315.855	0.052	1.110
113	4540.34	16	1.356	0.2	56.893	60.782	0.062	1.158

(*continued on next page*)

(*continued*)

Number	*Re*	*N*	D_f (mm)	φ	$\overline{Nu}$	Δp	*f*	*PEC*
114	5675.21	16	1.356	0.2	68.095	90.582	0.059	1.139
115	6810.52	16	1.356	0.2	79.095	125.438	0.057	1.126
116	7945.55	16	1.356	0.2	89.825	165.854	0.056	1.118
117	9078.43	16	1.356	0.2	100.360	210.932	0.054	1.111
118	10,215.79	16	1.356	0.2	110.907	262.554	0.053	1.106
119	11,350.76	16	1.356	0.2	121.340	317.178	0.052	1.105

Data availability

Data will be made available on request.

References

[1] S.K. Singh, V. Khan, R. Kacker, Thermal performance optimization of double pipe heat exchanger using novel wire coil helical inserts, Int. Commun. Heat Mass Transf. 162 (2025) 108624, 2025/03/01, https://doi.org/10.1016/j.icheatmasstransfer.2025.108624.

[2] M. Omidi, M. Farhadi, M. Jafari, A comprehensive review on double pipe heat exchangers, Appl. Therm. Eng. 110 (2017) 1075–1090, 2017/01/05, https://doi.org/10.1016/j.applthermaleng.2016.09.027.

[3] C. Shen, B. Zhang, D. Zhang, Y. Zhang, S. Wei, S. Yang, Experimental study on the parallel-flow heat pipe heat exchanger for energy saving in air conditioning, J. Build. Eng. 75 (2023) 106842, 2023/09/15, https://doi.org/10.1016/j.jobe.2023.106842.

[4] B. Hayat, W. Yafei, W. Yilin, H. Huwang, Z. Peng, Z. Yang, Investigation of heat transfer performance of double-walled pipes of heat exchanger for power plant applications, Int. Commun. Heat Mass Transf. 149 (2023) 107115, 2023/12/01, https://doi.org/10.1016/j.icheatmasstransfer.2023.107115.

[5] B. Ranjan Tamuli, S. Nath, D. Bhanja, Performance enhancement of a dual heat pipe array based evacuated tube solar water heater for north eastern India climatic condition: a numerical approach, Appl. Therm. Eng. 213 (2022) 118597, 2022/08/01, https://doi.org/10.1016/j.applthermaleng.2022.118597.

[6] H. Najafi Khaboshan, H.R. Nazif, The effect of multi-longitudinal vortex generation on turbulent convective heat transfer within alternating elliptical axis tubes with various alternative angles, Case Stud. Therm. Eng. 12 (2018) 237–247, 2018/09/01, https://doi.org/10.1016/j.csite.2018.04.013.

[7] O.G. Fadodun, O.O. Fadodun, A.H. Al-Tohamy, A. Kaood, Investigation of hydrothermal performance and irreversibility production rate of ferrosoferric oxide/water nanofluid in corrugated-converging pipes with varying geometry parameters, Int. J. Therm. Sci. 215 (2025) 109964, 2025/09/01, https://doi.org/10.1016/j.ijthermalsci.2025.109964.

[8] Y. Zhang, J. Liu, H. Cheng, T. Luan, T. Yang, H. Xue, Experimental study on the influence of surface modification methods of carbon fiber felt on the operation and heat transfer characteristics of loop heat pipes, Appl. Therm. Eng. 233 (2023) 121121, 2023/10/01, https://doi.org/10.1016/j.applthermaleng.2023.121121.

[9] S. Barati, A.R. Sajadi, B. Ghasemi, M. Bayareh, Heat transfer and fluid flow characteristics of a dual-tube heat exchanger with alternating flattened tubes, J. Therm. Anal. Calorim. 149 (23) (2024) 13967–13980, 2024/12/01, https://doi.org/10.1007/s10973-024-13614-6.

[10] S.A. Marzouk, F.A. Almehmadi, A. Aljabr, A. Kaood, Performance analysis of twisted tape inserts and nanofluids in double-pipe helical coil heat exchangers, J. Therm. Anal. Calorim. 150 (14) (2025) 11197–11211, 2025/07/01, https://doi.org/10.1007/s10973-025-14298-2.

[11] M.R. Salem, M.M. Ellaban, R.K. Ali, A.E. Elmohlawy, Experimental investigation of the performance attributes of a double pipe heat exchanger equipped with baffles of conventional or flower layouts, Appl. Therm. Eng. 253 (2024) 123771, 2024/09/15, https://doi.org/10.1016/j.applthermaleng.2024.123771.

[12] M.L.G. Ho, L.L. Tan, Y.M. Hung, C.S. Oon, Thermohydraulic and irreversibility analyses of swirl flows utilizing distorted radial fins: entropy generation and entransy dissipation evaluation, Int. J. Energy Res. 2023 (1) (2023) 5557828, 2023/01/01, https://doi.org/10.1155/2023/5557828.

[13] H. Najafi Khaboshan, H.R. Nazif, Heat transfer enhancement and entropy generation analysis of Al2O3-water nanofluid in an alternating oval cross-section tube using two-phase mixture model under turbulent flow, Heat Mass Transf. 54 (10) (2018) 3171–3183, 2018/10/01, https://doi.org/10.1007/s00231-018-2345-z.

[14] R. Karimpooremam, F. Poursaied, B. Keyvani, M. Razmi, R. Aghayari, D. Toghraie, S. Salahshour, Effect of using wire coils and aluminum oxide nanofluid on heat transfer in a double-pipe heat exchanger and predicting data with artificial neural networks, Case Stud. Therm. Eng. 71 (2025) 106232, 2025/07/01, https://doi.org/10.1016/j.csite.2025.106232.

[15] M.E. Nakhchi, J.A. Esfahani, K.C. Kim, Numerical study of turbulent flow inside heat exchangers using perforated louvered strip inserts, Int. J. Heat Mass Transf. 148 (2020) 119143, 2020/02/01, https://doi.org/10.1016/j.ijheatmasstransfer.2019.119143.

[16] Y. Wang, C.S. Oon, J.-J. Foo, M.-V. Tran, S.R. Nair, F.W. Low, Numerical investigation of thermo-hydraulic performance in an annular heat exchanger with sinusoidal vortex generators, J. Therm. Anal. Calorim. 148 (20) (2023) 10973–10990, 2023/10/01, https://doi.org/10.1007/s10973-023-12375-y.

[17] A.A. Dhavale, M.M. Lele, Numerical investigations on the impact of metallic foam configurations on heat transfer in double tube heat exchanger: a parametric approach, Numer. Heat Transf. A Appl. 86 (16) (2025) 5682–5734, 2025/08/18, https://doi.org/10.1080/10407782.2024.2333503.

[18] L. Ben Said, A.B.M. Ali, A.A. Alizadeh, K. Mausam, S. Dixit, R. Ali, M.A. Tashkandi, L. Kolsi, Development of improved heat transfer of double helical pipe heat exchangers using nano-fluids and perforated curved tabulators, Case Stud. Therm. Eng. 70 (2025) 106106, 2025/06/01, https://doi.org/10.1016/j.csite.2025.106106.

[19] A. El Maakoul, K. Feddi, S. Saadeddine, A. Ben Abdellah, M. El Metoui, Performance enhancement of finned annulus using surface interruptions in double-pipe heat exchangers, Energy Convers. Manag. 210 (2020) 112710, 2020/04/15, https://doi.org/10.1016/j.enconman.2020.112710.

[20] X. Luo, W. Li, L. Zhang, M. Zeng, J.J. Klemeš, Q. Wang, Effects evaluation of fin layouts and configurations on discharging performance of double-pipe thermochemical energy storage reactor, Energy 282 (2023) 128821, 2023/11/01, https://doi.org/10.1016/j.energy.2023.128821.

[21] A. El Maakoul, A. Laknizi, S. Saadeddine, A. Ben Abdellah, M. Meziane, M. El Metoui, Numerical design and investigation of heat transfer enhancement and performance for an annulus with continuous helical baffles in a double-pipe heat exchanger, Energy Convers. Manag. 133 (2017) 76–86, 2017/02/01, https://doi.org/10.1016/j.enconman.2016.12.002.

[22] W. Haw, C.S. Oon, E.V. Lau, Analysis of hydrodynamics and thermal–hydraulic performance of twisted angle fins within an annular conduit, J. Therm. Anal. Calorim. 150 (1) (2025) 377–394, 2025/01/01, https://doi.org/10.1007/s10973-024-13680-w.

[23] M.R. Shaeri, M. Yaghoubi, Thermal enhancement from heat sinks by using perforated fins, Energy Convers. Manag. 50 (5) (2009) 1264–1270, 2009/05/01, https://doi.org/10.1016/j.enconman.2009.01.021.

[24] Y. Shi, C. Liu, H. Chen, Y. Yue, M. Li, Impact of corrugated fins on flow and heat transfer performance in medium-deep coaxial underground heat exchangers, Energies 18 (9) (2025), https://doi.org/10.3390/en18092212.

[25] W. Haw, C.S. Oon, E.V. Lau, Thermal-hydraulic and hydrodynamic analysis of twisted fins in a double-pipe heat exchanger, Results Eng. 26 (2025) 104642, 2025/06/01, https://doi.org/10.1016/j.rineng.2025.104642.

[26] Z. Yan, C.S. Oon, B.T. Tan, J.B. Ooi, Geometric design and optimization of extended surfaces for enhanced heat transfer: a comprehensive review, Results Eng. 27 (2025) 106227, 2025/09/01, https://doi.org/10.1016/j.rineng.2025.106227.

[27] M.R. Shaeri, T.-C. Jen, The effects of perforation sizes on laminar heat transfer characteristics of an array of perforated fins, Energy Convers. Manag. 64 (2012) 328–334, 2012/12/01, https://doi.org/10.1016/j.enconman.2012.05.002.

[28] M. Sheikholeslami, D.D. Ganji, Heat transfer improvement in a double pipe heat exchanger by means of perforated turbulators, Energy Convers. Manag. 127 (2016) 112–123, 2016/11/01, https://doi.org/10.1016/j.enconman.2016.08.090.

[29] Y. Wang, C.S. Oon, J.-J. Foo, M.-V. Tran, S.R. Nair, F.W. Low, Numerical investigation of thermo-hydraulic performance utilizing clove-treated graphene nanoplatelets nanofluid in an annular passage with perforated curve fins, Results Eng. 17 (2023) 100848, 2023/03/01, https://doi.org/10.1016/j.rineng.2022.100848.

[30] K. Song, Y. He, Q. Zhang, X. Wu, A. He, Q. Hou, Thermal performance promotion of a novel double-tube heat exchanger by helical fin with perforations, Int. Commun. Heat Mass Transf. 150 (2024) 107189, 2024/01/01, https://doi.org/10.1016/j.icheatmasstransfer.2023.107189.

[31] Y. Ying-De, C. Jun, H. Yi-Fu, N. Ya-Shan, Q. Ling-Yun, Z. Chen-Hao, Z. Jia-Yi, H. Xin-Hao, L. Shi-Jie, T. Ai-Min, Shell-side flow resistance and enhanced heat transfer for a novel twisted elliptical tube double-pipe heat exchanger, Int. Commun. Heat Mass Transf. 172 (2026) 110686, 2026/03/01, https://doi.org/10.1016/j.icheatmasstransfer.2026.110686.

[32] R. Verzicco, K.R. Sreenivasan, A comparison of turbulent thermal convection between conditions of constant temperature and constant heat flux, J. Fluid Mech. 595 (2008) 203–219, https://doi.org/10.1017/S0022112007009135.

[33] A. Mosyak, E. Pogrebnyak, G. Hetsroni, Effect of constant heat flux boundary condition on wall temperature fluctuations, J. Heat Transf. 123 (2) (2000) 213–218, https://doi.org/10.1115/1.1345886.

[34] O. Almatar AbdRabbuh, C.S. Oon, S.N. Kazi, A.H. Abdelrazek, W. Ahmed, A. R. Mallah, A. Badarudin, I.A. Badruddin, S. Kamangar, An experimental investigation of eco-friendly treated GNP heat transfer growth: circular and square conduit comparison, J. Therm. Anal. Calorim. 145 (1) (2021) 139–151, 2021/07/01, https://doi.org/10.1007/s10973-020-09652-5.

[35] S. Barati, A.R. Sajadi, B. Ghasemi, Heat transfer performance and flow characteristics of oil-ZnO nanofluid in an alternating flattened tube in dual-tube heat exchanger: experimental and numerical approaches, Int. J. Therm. Sci. 204 (2024) 109180, 2024/10/01, https://doi.org/10.1016/j.ijthermalsci.2024.109180.

[36] G. Ji, J. Dong, M. Zhang, Y. Lu, The basic theory of CFD governing equations and the numerical solution methods for reactive flows, in: G. Ji, J. Dong (Eds.), Computational Fluid Dynamics - Recent Advances, New Perspectives and Applications, IntechOpen, London, 2023.

[37] B.A. Kader, Temperature and concentration profiles in fully turbulent boundary layers, Int. J. Heat Mass Transf. 24 (9) (1981) 1541–1544, 1981/09/01, https://doi.org/10.1016/0017-9310(81)90220-9.

[38] W.M. Kays, Turbulent Prandtl number—where are we? J. Heat Transf. 116 (2) (1994) 284–295, https://doi.org/10.1115/1.2911398.

[39] H.N. Khaboshan, E. Yousefi, J. Svorcan, Analysis of the turbulent boundary layer and skin-friction drag reduction of a flat plate by using the micro-blowing technique, J. Appl. Mech. Tech. Phys. 63 (3) (2022) 425–436, 2022/06/01, https://doi.org/10.1134/S0021894422030075.

[40] ANSYS, FLUENT Theory Guide, Release 22.1, ANSYS Inc, 2022.

[41] Z. Esmaeili, S.M. Vahidhosseini, S. Rashidi, A novel design of double pipe heat exchanger with innovative turbulator inside the shell-side space, Int. Commun. Heat Mass Transf. 155 (2024) 107523, 2024/06/01, https://doi.org/10.1016/j.icheatmasstransfer.2024.107523.

[42] N.T. Ravi Kumar, P. Bhramara, A. Kirubeil, L. Syam Sundar, M.K. Singh, A.C. M. Sousa, Effect of twisted tape inserts on heat transfer, friction factor of Fe3O4 nanofluids flow in a double pipe U-bend heat exchanger, Int. Commun. Heat Mass Transf. 95 (2018) 53–62, 2018/07/01, https://doi.org/10.1016/j.icheatmasstransfer.2018.03.020.

[43] H. Peng, M. Li, F. Hu, S. Feng, Performance analysis of absorber tube in parabolic trough solar collector inserted with semi-annular and fin shape metal foam hybrid structure, Case Stud. Therm. Eng. 26 (2021) 101112, 2021/08/01, https://doi.org/10.1016/j.csite.2021.101112.

[44] R.L. Webb, N.-H. Kim, Principles of Enhanced Heat Transfer, Taylor Francis, New York, 1994.

[45] D. Hao, K. Liu, B. Cai, W. Cai, Numerical analysis and performance evaluation of a petal-shaped helical tube double-pipe heat exchanger for steam generation in concentrated solar power systems, Appl. Therm. Eng. 280 (2025) 128393, 2025/12/01, https://doi.org/10.1016/j.applthermaleng.2025.128393.

[46] F. Ejaz, N.A.A. Qasem, S.M. Zubair, Thermal-hydraulic performance evaluation of airside of wavy fin compact heat exchangers under wet conditions, Int. Commun. Heat Mass Transf. 156 (2024) 107685, 2024/08/01, https://doi.org/10.1016/j.icheatmasstransfer.2024.107685.

[47] V. Gnielinski, Turbulent heat transfer in annular spaces—a new comprehensive correlation, Heat Transf. Eng. 36 (9) (2015) 787–789, 2015/06/13, https://doi.org/10.1080/01457632.2015.962953.

[48] B.S. Petukhov, Heat transfer and friction in turbulent pipe flow with variable physical properties, Adv. Heat Tran. 6 (1970) 503–564, 1970/01/01, https://doi.org/10.1016/S0065-2717(08)70153-9.

[49] M. Hosseini, R. Sadri, S.N. Kazi, S. Bagheri, N. Zubir, C. Bee Teng, T. Zaharinie, Experimental study on heat transfer and thermo-physical properties of covalently functionalized carbon nanotubes nanofluids in an annular heat exchanger: a green and novel synthesis, Energy Fuel 31 (5) (2017) 5635–5644, 2017/05/18, https://doi.org/10.1021/acs.energyfuels.6b02928.

[50] H. Schlichting, K. Gersten, Boundary-Layer Theory, 2017, https://doi.org/10.1007/978-3-662-52919-5.

[51] H.K. Versteeg, W. Malalasekera, An Introduction to Computational Fluid Dynamics: The Finite Volume Method, 2nd ed., Pearson Education, 2007.

[52] M.S. Kumar, S. Abraham, Experimental and numerical studies of detailed heat transfer and flow characteristics in the rib turbulated annulus of a double pipe heat exchanger, Int. J. Therm. Sci. 207 (2025) 109382, 2025/01/01, https://doi.org/10.1016/j.ijthermalsci.2024.109382.

[53] T. Ambreen, M.-H. Kim, Effect of fin shape on the thermal performance of nanofluid-cooled micro pin-fin heat sinks, Int. J. Heat Mass Transf. 126 (2018) 245–256, 2018/11/01, https://doi.org/10.1016/j.ijheatmasstransfer.2018.05.164.

[54] M.I. Hasan, Investigation of flow and heat transfer characteristics in micro pin fin heat sink with nanofluid, Appl. Therm. Eng. 63 (2) (2014) 598–607, 2014/02/22, https://doi.org/10.1016/j.applthermaleng.2013.11.059.